Distinct cytoskeletal proteins define zones of enhanced cell wall synthesis in *Helicobacter pylori*

Jennifer A. Taylor[1,2], Benjamin P. Bratton[3,4], Sophie R. Sichel[2,6], Kris M. Blair[2,7], Holly M. Jacobs[2,7], Kristen E. DeMeester[8], Erkin Kuru[9], Joe Gray[10], Jacob Biboy[11], Michael S. VanNieuwenhze[12], Waldemar Vollmer[11], Catherine L. Grimes[8,13], Joshua W. Shaevitz[3,5], Nina R. Salama[1,2,6,7]

1 Department of Microbiology, University of Washington, Seattle, WA, USA

2 Human Biology Division, Fred Hutchinson Cancer Research Center, Seattle, WA, USA

3 Lewis-Sigler Institute of Integrative Genomics, Princeton University, Princeton, NJ, USA

4 Department of Molecular Biology, Princeton University, Princeton, NJ, USA

5 Department of Physics, Princeton University, Princeton, NJ, USA

6 Molecular Medicine and Mechanisms of Disease Graduate Program, University of Washington, Seattle WA, USA

7 Molecular and Cellular Biology Graduate Program, University of Washington, Seattle, WA, USA

8 Department of Chemistry and Biochemistry, University of Delaware, Newark, DE, USA.

9 Department of Genetics, Harvard Medical School, Boston, MA, USA

10 Institute for Cell and Molecular Biosciences, Newcastle University, Newcastle upon Tyne, UK

11 Centre for Bacterial Cell Biology, Institute for Cell and Molecular Biosciences, Newcastle University, Newcastle upon Tyne, UK

12 Department of Chemistry, Indiana University, Bloomington, IN, USA

13 Department of Biological Sciences, University of Delaware, Newark, DE, USA

Correspondence:

Nina R. Salama

nsalama@fredhutch.org

Abstract

Helical cell shape is necessary for efficient stomach colonization by *Helicobacter pylori*, but the molecular mechanisms for generating helical shape remain unclear. We show that the helical centerline pitch and radius of wild-type *H. pylori* cells dictate surface curvatures of considerably higher positive and negative Gaussian curvatures than those present in straight- or curved-rod bacteria. Quantitative 3D microscopy analysis of short pulses with either *N*-acetylmuramic acid or D-alanine metabolic probes showed that cell wall growth is enhanced at both sidewall curvature extremes. Immunofluorescence revealed MreB is most abundant at negative Gaussian curvature, while the bactofilin CcmA is most abundant at positive Gaussian curvature. Strains expressing CcmA variants with altered polymerization properties lose helical shape and associated positive Gaussian curvatures. We thus propose a model where CcmA and MreB promote PG synthesis at positive and negative Gaussian curvatures, respectively, and that this patterning is one mechanism necessary for maintaining helical shape.

Introduction

Helicobacter pylori is a helical Gram-negative bacterium that colonizes the human stomach and can cause stomach ulcers and gastric cancers (Correa, 1988). Helical cell shape is necessary for efficient stomach colonization (Bonis et al., 2010; Sycuro et al., 2012, 2010), underscoring its importance. *H. pylori* is a main model organism for studying helical cell shape, in part because it is a genetically tractable organism with a compact genome that minimizes redundancy (Tomb et al., 1997). Key non-redundant, non-essential contributors to cell shape have been identified, but the question of how they enable *H. pylori* to be helical remains largely unsolved.

As is the case for most bacteria (Höltje, 1998), the structure of the *H. pylori* peptidoglycan (PG) cell wall (sacculus) is ultimately responsible for the shape of the cell; purified cell walls maintain helical shape (Sycuro et al., 2010). PG is a polymer of alternating *N*-acetylglucosamine (GlcNAc) and *N*-acetylmuramic acid (MurNAc) with an attached peptide stem that can be crosslinked to a peptide stem of an adjacent PG strand (Figure 1 - supplement 1). Crosslinked PG strands form the cell wall, a large mesh-like macromolecule that surrounds the cell and counteracts the cell's turgor pressure (Höltje, 1998; Typas et al., 2012). The PG monomer is synthesized in the cytoplasm and subsequently flipped across the inner membrane and incorporated into the existing PG by the glycosyltransferase activities of penicillin binding proteins (PBPs) and perhaps shape, elongation, division and sporulation (SEDS) proteins and the transpeptidation activities of PBPs (Meeske et al., 2016; Sauvage et al., 2008).

Helical cell shape maintenance in *H. pylori* requires a suite of both PG-modifying enzymes (Csd1, Csd3/HdpA, Csd4, Csd6) to remodel the cell wall and non-enzymatic proteins (Csd2, Csd5, CcmA) that may act as scaffolds or play other structural roles (Bonis et al., 2010; Sycuro et al., 2013, 2012, 2010). One of the non-enzymatic proteins is the putative bactofilin CcmA. Bactofilins are bacteria-specific cytoskeletal proteins with diverse functions, including playing a role in stalk elongation in *Caulobacter crescentus* (Kühn et al., 2010) and helical pitch modulation in *Leptospira biflexa* (Jackson et al., 2018). CcmA loss in *H. pylori* results in rod-shaped cells with minimal sidewall curvature (Sycuro et al., 2010). Recently CcmA was shown to co-purify with Csd5 and the PG biosynthetic enzyme MurF (Blair et al., 2018), suggesting CcmA may influence cell wall growth.

Patterning PG synthesis has been shown to be an important mechanism for cell shape maintenance in several model organisms. In the rod-shaped *Escherichia coli*, MreB helps direct synthesis preferentially to sites at or below zero Gaussian curvature. This growth pattern promotes rod shape by accelerating

growth at dents and restricting growth at bulges along the sidewall, thereby enforcing diameter control (Bratton et al., 2018; Ursell et al., 2014). In the Gram-positive *Bacillus subtilis*, MreB filaments have been shown to move in paths oriented approximately perpendicular to the long axis of rod shaped cells. The relative organization of path orientations decreases with an increase in rod diameter, suggesting that filament orientation is sensitive to changes in cell surface curvatures (Hussain et al., 2018).

Here, we demonstrate that the surface of helical *H. pylori* cells is characterized by large regions of both positive and negative Gaussian curvature. To investigate how *H. pylori* achieves diameter control while simultaneously maintaining sidewall curvature, we employed two metabolic probes to investigate PG synthesis patterning in *H. pylori*. Using superresolution microscopy and 3D quantitative image analysis, we show that synthesis is enhanced at negative Gaussian curvature as well as at a limited range of positive Gaussian curvatures. We furthermore investigate the localization of cytoskeletal proteins MreB and CcmA. We demonstrate that, as in straight-rod shaped cells, MreB is enriched at negative curvature. CcmA is enriched at the window of positive Gaussian curvatures where enhanced synthesis is observed. We propose that both MreB and CcmA help recruit PG synthesis activity locally and that PG synthesis patterning is one mechanism that plays a fundamental role in helical cell shape maintenance.

Results

Helical cells maintain areas of positive and negative Gaussian curvature on the sidewall

Unlike straight rod-shaped bacteria, helical *H. pylori* cells maintain distinct and diverse cell surface curvatures along the sidewall (Figure 1 and Figure 2). To characterize the cell surface curvature features of *H. pylori* in detail, we stained permeabilized cells with fluorescent wheat germ agglutinin (WGA), which binds GlcNAc and thus labels the cell wall. Since the dimensions of *H. pylori* cells (1.5-3.5 µm in length and 0.45 µm in diameter (Figure 3)) are near the limit of light microscopy resolution, we employed 3D structured illumination microscopy (SIM) to more clearly resolve cells in three dimensions (Figure 1A). We adapted previous image processing software (Bartlett et al., 2017; Morgenstein et al., 2015) to accommodate characteristic SIM artifacts and enhanced resolution in order to generate a 3D triangular meshwork surface with roughly 30 nm precision from the SIM z-stack images (Figure 1A and B, matched SIM image volumes and surface reconstructions). Display of the Gaussian curvature, which is the product of the two principal curvatures, at each point on the meshwork revealed distinct curvatures on opposite sides of helical cells (Figure 1B). Using Gaussian curvature allows us to focus on local curvature geometry. We operationally define the minor helical axis as the shortest helical path along the sidewall within the zone of moderate negative curvature (minor helical axis area, -15 to -5 μm^{-2}, blue),

and define the major axis as the path opposite the minor helical axis, which resides within the zone of moderate positive curvature (major helical axis area, 5 to 15 μm^{-2}, red) (Figure 1C). The cell poles are characterized by high positive curvature (>15 μm^{-2}, gray).

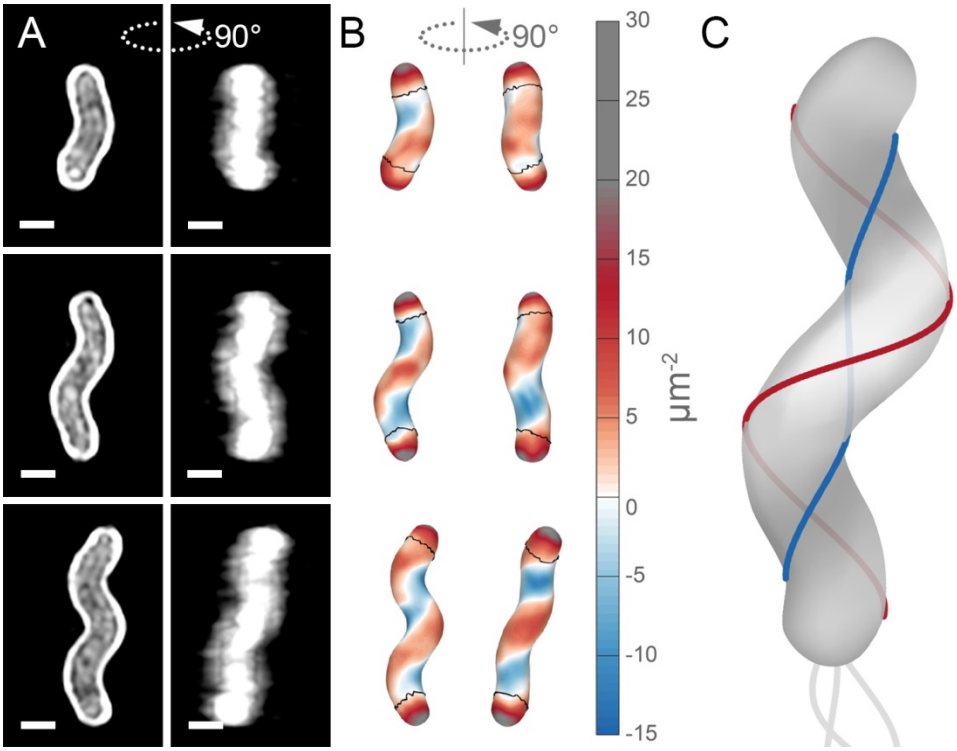

Figure 1. Helical cell surface feature areas of distinct curvatures. (**A**) 3D SIM images of individual *H. pylori* cells stained with fluorescent wheat germ agglutinin (WGA). Top-down view (left) and 90-degree rotation about the long axis (right). Scale bar = 1 μm; images from one experiment. (**B**) Corresponding views of computational surface reconstructions of cells in A. with Gaussian curvature plotted (scale at right - blue: moderate negative; white: zero; red: moderate positive; gray: high positive). Computationally-defined polar regions are delineated by the thin black line. Polar regions correspond to regions whose centerline points are within 0.75 of a cell diameter to the terminal pole positions. (**C**) Schematic of minor (blue line) and major (red line) helical axes.

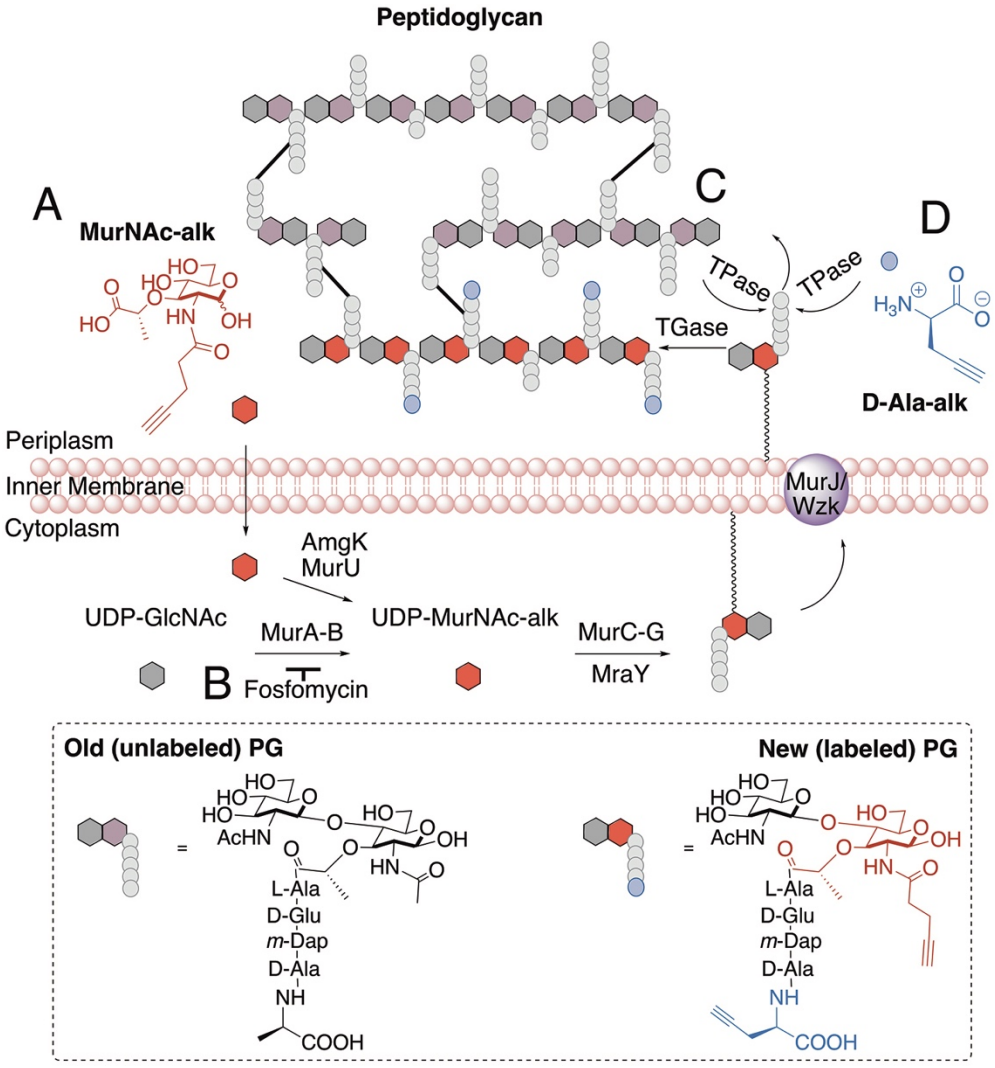

Figure 1 - figure supplement 1. Schematic of PG synthesis and incorporation of PG metabolic probes. (**A**) MurNAc-alk diffuses across the cell membrane and is converted into UDP-MurNAc-alk, which can then be used in the synthesis of PG precursors. (**B**) Fosfomycin inhibits the conversion of UDP-GlcNAc to UDP-MurNAc. Addition of exogenous MurNAc allows the cell to bypass this step and survive when treated with fosfomycin. To incorporate the new PG monomer into the cell wall, transglycosylases (TGase) polymerize the glycan strand. (**C**) To link the new strand to the existing PG, transpeptidases (TPase) form a crosslink between the tetra position D-Ala of the new peptide stem and the *m*-Dap of a nearby peptide stem, resulting in loss of the penta position D-Ala of the new peptide stem. (**D**) In a reaction similar to forming a crosslink, TPases can replace the penta position D-Ala with D-Ala-alk. In our experiments labeling PG incorporation, we labeled cells with either MurNAc-alk or D-Ala-alk.

Our image reconstruction method performs faithful reconstructions of straight- and curved-rod cells (Figure 2, inset). To compare the surface curvatures maintained by helical (wild-type), curved-rod (Δ*csd2*), and straight-rod (Δ*csd6*) cells, we pooled reconstructions of hundreds of non-septating cells for each genotype and plotted a histogram of the proportion of surface curvature points with a given Gaussian curvature value (Figure 2). All three cell shapes share a tail of high positive curvatures from the cell poles (Figure 2A, right of the dotted line). In order to study the sidewall alone, we developed an algorithm to computationally define and exclude poles (Figure 1B, black lines). With the poles removed, the extended tail disappears for each cell shape. In contrast to the other shapes, helical cells have a large proportion of sidewall area with curvatures less than -5 μm^{-2} and an even larger proportion with curvatures greater than 5 μm^{-2} (Figure 2B). Rather than having a unimodal distribution, helical cells have a multimodal distribution that includes an apparent peak at negative curvature and another at positive curvature.

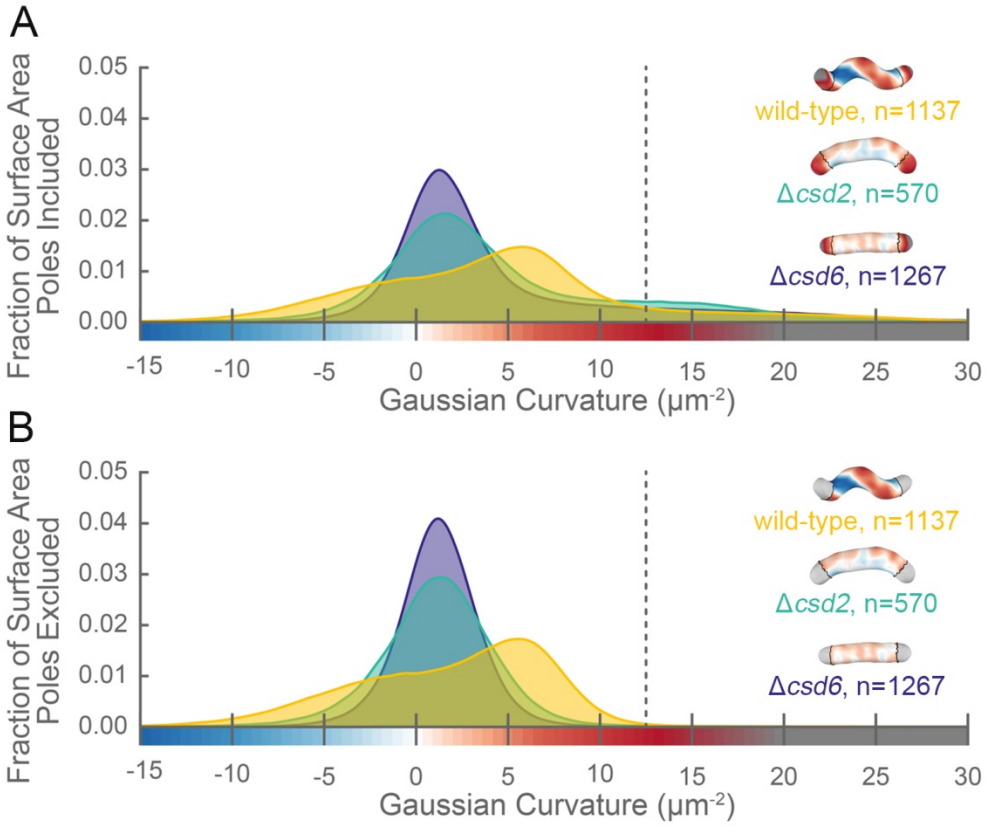

Figure 2. The distribution of surface Gaussian curvature for helical cells is distinct from that of curved- and straight-rod cells. Smooth histograms of the distribution of surface Gaussian curvatures for a population of cells (wild-type helical, yellow, n=1137; curved-rod Δ*csd2*, teal, n=570; straight-rod Δ*csd6*, indigo, n=1267) with poles included (**A**) or sidewall only (**B**, poles excluded). The region to the right of

the dotted vertical lines corresponds to curvatures contributed almost exclusively by the poles. Histograms are derived using a bin size of 0.2 μm^{-2}. Example computational surface reconstructions (top right of each histogram) of a wild-type helical, curved-rod Δ*csd2*, and straight-rod Δ*csd6* cell with Gaussian curvatures displayed as in Figure 1. The data represented are from one experiment.

The sidewall curvature distribution informed us about the overall types of surface curvature wild-type cells need to achieve, but was not sufficient to let us directly compare the surface properties of the major and minor axes, specifically the relative lengths of the major and minor axes and the average Gaussian curvature along both axes. To achieve this, we needed to find the major and minor axis on each reconstructed cell surface. While cells in our experiments appear helical, in reality they have surface imperfections and centerlines with kinks, bends, or variation in pitch along the centerline (Sycuro et al., 2010). We therefore limited ourselves to considering the relative length of the major and minor helical axes of a population of simulated, idealized cells, each of which mimics a cell from the wild-type population described in Figure 2 (for full details see Appendix 1). In brief, to both derive the cell shape parameters necessary to generate the simulated cells and to further characterize the 3D shape parameters of the wild-type population, we measured the cell lengths from one pole to the other along the curved centerlines (Figure 3A and C, gray); the diameters of the cells (Figure 3A and C, purple); the helical pitches of the centerlines (Figure 3A and C, pink); and the helical diameters of the centerlines (Figure 3A and C, green).Wild-type cells are 2.5 ± 0.5 µm long and 0.45 ± 0.02 µm in diameter, have a helical pitch of 1.7 ± 1 µm, and have a helical diameter of 0.3 ± 0.1 µm (mean ± standard deviation, Figure 3C-F). These parameters are derived from a subset of the wild-type population that can be modeled as a uniform helix (Figure 3 - supplement 1 and 2). The distribution of cell lengths, diameters, and surface curvatures of the subset closely match that of the whole population (Figure 3 - supplement 1C-E).

Using the simulated counterparts to these cells, we determined that the average major to minor length ratio is 1.69±0.16, meaning that the major axis is on average 70% longer than the minor axis (Figure 3G). We also determined from the simulated cells that the average Gaussian curvature at the major axis is 5±1 μm^{-2}, and the average Gaussian curvature at the minor axis is -11±4 μm^{-2} (Figure 3H).

We next used our simulation framework to explore how the four helical-rod shape parameters affect the length ratio of the major to minor helical axes. Changes in cell length and cell diameter had almost no effect, whereas increasing the helical diameter or decreasing the helical pitch increased the relative

length of the major axis (Figure 3 - supplement 3, right column), consistent with the idea that a helix is formed by differential expansion of the major and minor axes. We then investigated how each of these parameters influences the distribution of surface curvatures along the sidewall. We began with a cell simulated from the population average of all four parameters (cell length, cell diameter, helical pitch, and helical diameter), and changed each property individually within the range of variation represented in the wild-type population (± 1.5 standard deviations) while holding the other three constant (Figure 3 - supplement 3 and 4). Each of the dashed colored lines in Figure 3C-F correspond to the parameters used to simulate these altered cell shapes. Changing cell length had a negligible impact on the distribution of surface curvatures along the sidewall (Figure 3 - supplement 3A). Decreasing the cell diameter had a relatively small effect given the narrow distribution of cell diameters observed in the wild-type population (Figure 3 - supplement 3B). Changing the two parameters describing the properties of the helix had a larger impact on the distribution of Gaussian curvatures. Decreasing the pitch resulted in a helix with tighter coils and a greater distance between the peak of negative and positive Gaussian surface curvatures (Figure 3 - supplement 3C). Increasing the helical diameter resulted in cells that looked less like straight-rod cells and had a greater distance between the peak of negative and positive Gaussian surface curvatures (Figure 3 - supplement 3D). In holding with the Gauss-Bonnet theorem, cells had a greater proportion of sidewall area with positive Gaussian curvature than with negative, and the magnitude of the positive Gaussian curvature was less than that of the negative Gaussian curvature.

Having established the substantial difference in the length of the major and minor axes, we wondered if differential synthesis at these cellular landmarks might help explain helical shape maintenance. Although it is not currently possible to computationally define the helical axes on surface reconstructions of actual cells due to their imperfections, our data indicate that we can use Gaussian curvature of 5 μm^{-2} and -11 μm^{-2} as a proxy for the major and minor axes, respectively, in population level data.

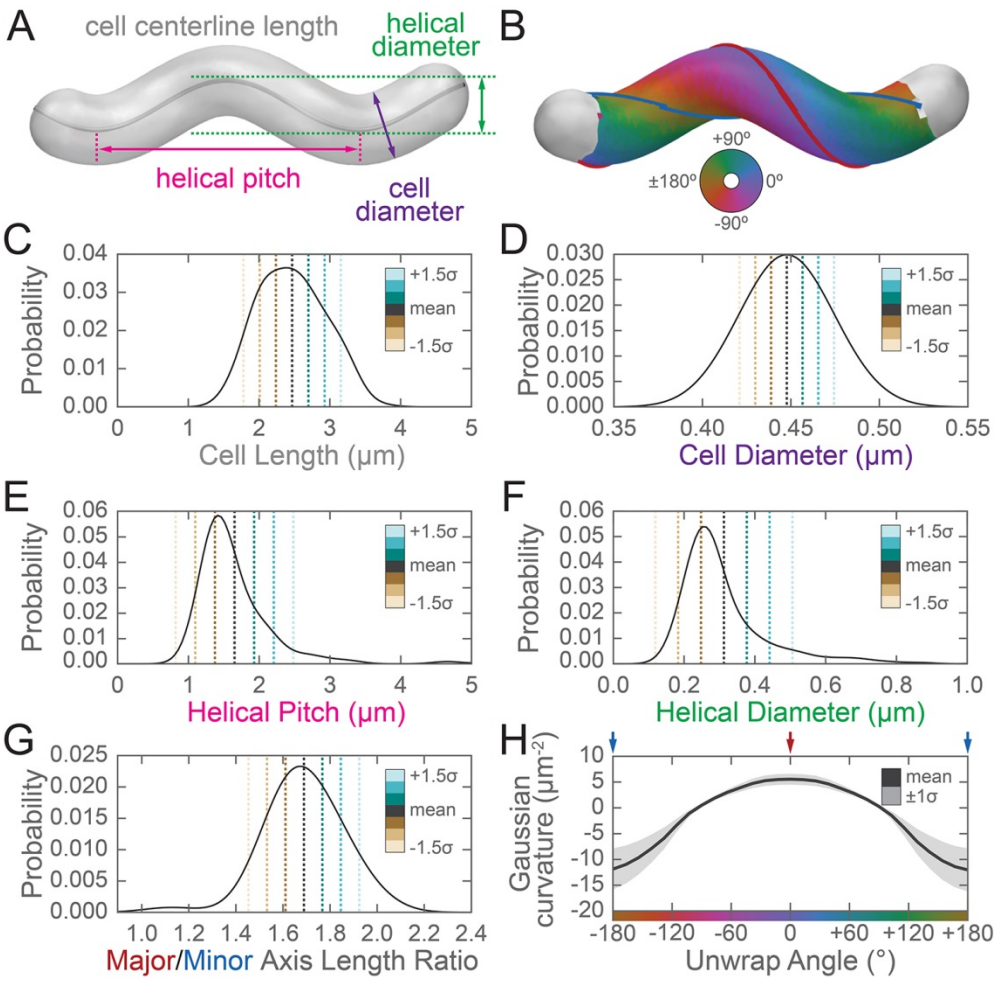

Figure 3. Three-dimensional shape properties of a wild-type helical population. Analysis of the wild-type population in Figure 2 from the 231 wild-type cells for which the cell centerline was well-fit by a helix. (**A**) Schematic of helical-rod shape parameters (cell centerline length, gray; cell diameter, purple; helical pitch, pink; and helical diameter, green). (**B**) Example cell with helical coordinate system and the major (red line, 0°) and minor (blue line, 180°) helical axes shown on the cell sidewall. Population distributions of (**C**) cell centerline lengths, (**D**) average cell diameters, (**E**) helical pitch, (**F**) helical diameter, (**G**) major to minor axis length ratio, and (**H**) the average Gaussian curvature for a given helical coordinate system unwrap angle. Colored dotted lines in (**C**-**G**) indicate the mean ±1.5 standard deviations in 0.5 standard deviation steps. Shaded line in (**H**) indicates ±1 standard deviation about the mean. Distributions of parameters (C-D) are from real cells, parameters (E-F) are from helical centerline fits, and properties (G-H) are measured from the matched synthetic cell sidewalls.

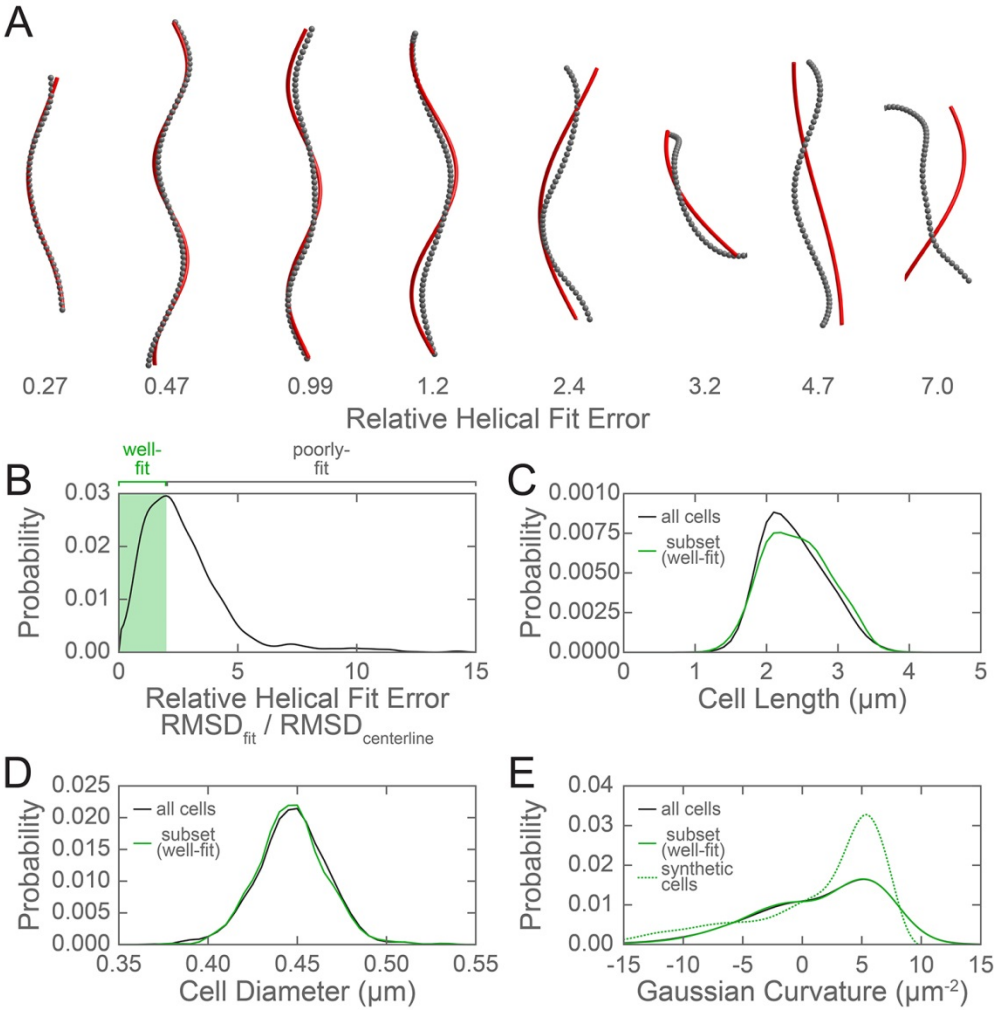

Figure 3 - figure supplement 1. Evaluation of the subset of the wild-type population used to generate synthetic cells. (**A**) Example cell centerlines (gray dots) and calculated helical fits (red lines), arranged from good (left) to poor (right) fit. (**B**) Histogram of the relative helical fit error for each of the cells from the wild-type population shown in Figure 2. Shaded green box indicates well-fit centerlines with a relative helical fit error below the selected threshold of 2, which were used for further analysis. Comparison of the population distribution of (**C**) cell lengths and (**D**) average cell diameters for the entire wild-type population (black line) and the subset of cells with a centerline that was well fit by a helix (green). (**E**) Comparison of the population cell surface Gaussian curvature distribution for the entire wild-type population (black line), the selected subset of wild-type cells (green line), and the synthetic cells generated based on the cell centerline helical fits of the selected subset (dotted green line).

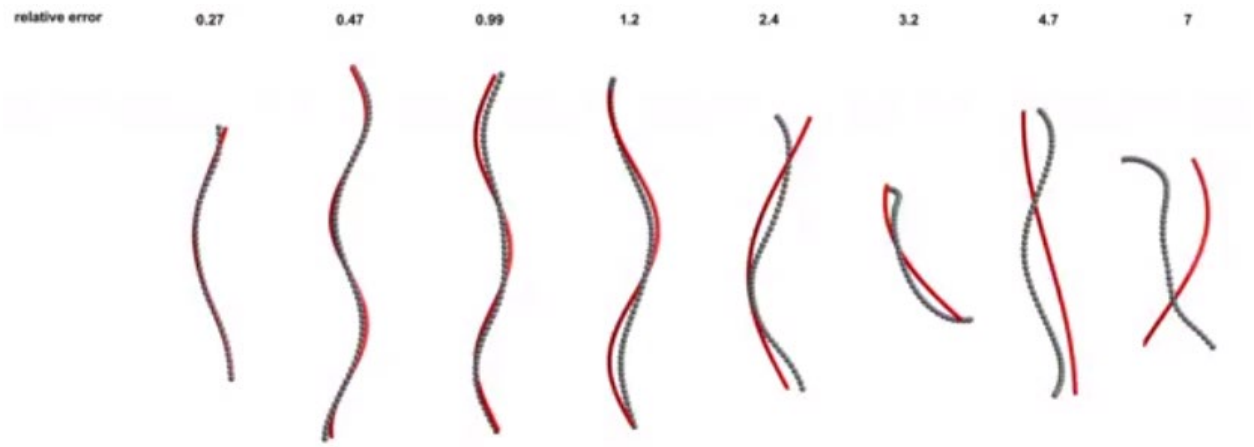

214

215 **(placeholder for .avi)**

216 **Figure 3 - figure supplement 2. Rotation of example cell centerlines (gray dots) and calculated helical**
217 **fits (red lines), arranged from good (left) to poor (right) fit from Figure 3- figure supplement 1A.**

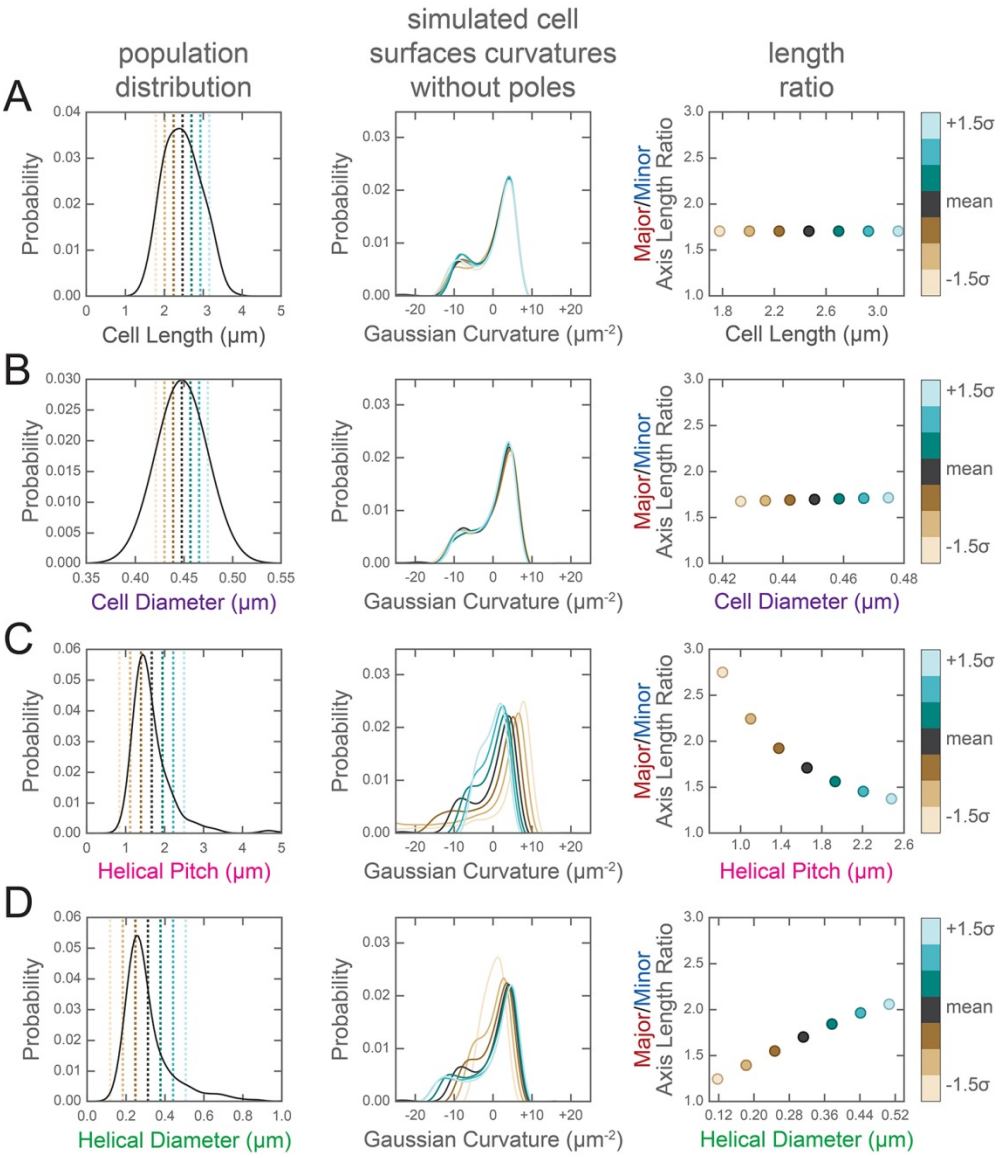

Figure 3 - figure supplement 3. Change in the distribution of cell surface Gaussian curvatures based on modulating helical rod parameters. Left column, distribution of population helical rod parameters from Figure 3C-F. Center column, Gaussian surface curvature distribution of the synthetic cells in Figure 3 – figure supplement 2 without poles for (**A**) cell centerline length, (**B**) cell diameter, (**C**) helical pitch, and (**D**) helical radius modulated to the mean ±1.5 standard deviations in 0.5 standard deviation increments. Right column, ratio of major to minor axis length vs. (**A**) cell centerline length, (**B**) cell diameter, (**C**) helical pitch, and (**D**) helical radius modulated to the mean ±1.5 standard deviations in 0.5 standard deviation increments. As shown in the color bar at the far right, data for the mean cell data are plotted in gray; data for cells generated with a parameter modulated to a value greater than the mean are shown in blue tones; and data for cells generated with a parameter modulated to a value less than the mean are shown in tan tones.

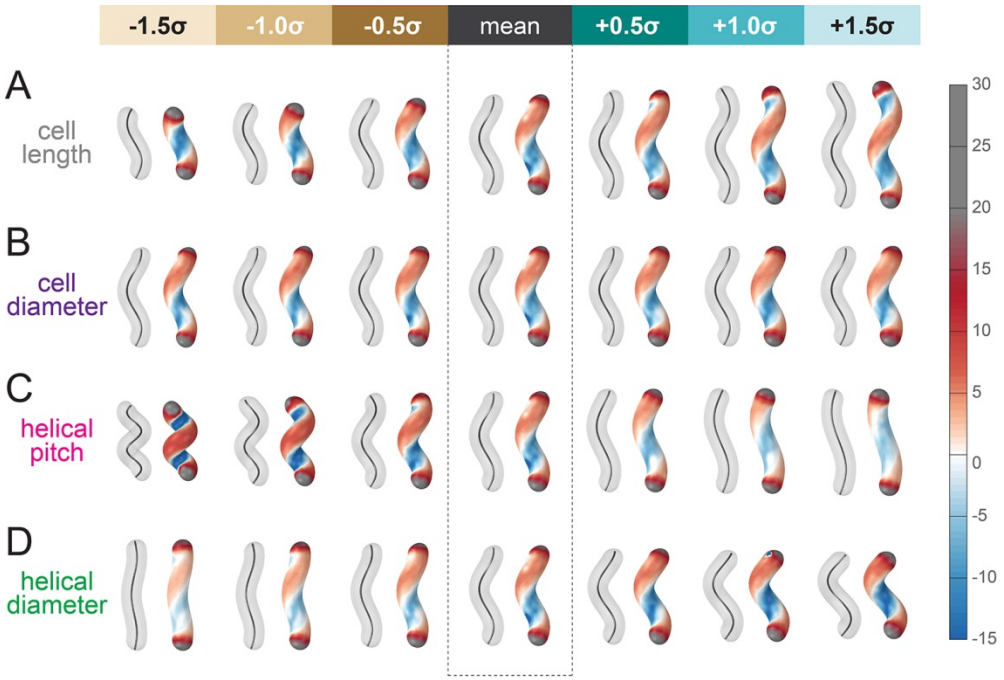

Figure 3 - figure supplement 4. Simulated helical cells demonstrating how variation in helical parameters alters surface Gaussian curvature. Cell centerline (paired cells, left) and cell surface Gaussian curvatures (paired cells, right) of synthetic, idealized cells with parameters taken from the distribution of wild-type shapes. The central pair of cells in each row was generated using the average value for each shape parameter shown in Figure 3 and is the same for all rows. Each of the parameters (**A**) cell centerline length, (**B**) cell diameter, (**C**) helical pitch, and (**D**) helical radius is increased (right of mean cell pair) and decreased (left of mean cell) up to 1.5 standard deviations in 0.5 standard deviation increments while leaving the remaining three parameters fixed at the population mean.

H. pylori can incorporate modified D-alanine and modified MurNAc into peptidoglycan

Since a helical cell must maintain large regions of positive and of negative curvatures, we hypothesized that *H. pylori* may have a different growth pattern than that of *E. coli*, where the majority of the sidewall regions have Gaussian curvature near zero. To determine where new PG is preferentially inserted, we used two metabolic probes of PG incorporation. First, we attempted labeling wild-type cells with MurNAc-alkyne (MurNAc-alk), but *H. pylori* is unable to readily use exogenous MurNAc. We then engineered a strain, HJH1, containing recycling enzymes AmgK and MurU from *Pseudomonas putida* (Gisin et al., 2013) at the *rdxA* locus, a neutral locus routinely used for expression of genes in *H. pylori* (Goodwin et al., 1998; Smeets et al., 2000). These enzymes convert MurNAc into UDP-MurNAc, which can then be used to form PG subunit precursors (Figure 1 - supplement 1). To verify that HJH1 can indeed use exogenous MurNAc, we assayed rescue from fosfomycin treatment. Fosfomycin blocks the first committed step in PG precursor synthesis by preventing the conversion of UDP-GlcNAc into UDP-MurNAc (Figure 1 - supplement 1). We determined the minimum inhibitory concentration (MIC) of fosfomycin of our strain to be 25 μg/ml (Figure 4 - supplement 1). Supplementation with 4 mg/ml MurNAc partially rescued growth of HJH1 in the presence of 50 μg/ml fosfomycin, but not the parental strain (LSH108) (Figure 4A).

To verify that clickable MurNAc-alk is indeed incorporated into the cell wall, we purified sacculi from HJH1 labeled with MurNAc-alk for six doublings for MS/MS analysis. We positively identified MurNAc-alk-pentapeptide and MurNAc-alk-tetra-pentapeptide, the most abundant monomeric and dimeric species in the *H. pylori* cell wall, (Figure 4B and supplement 2), as well as in less-abundant species (Table 1), confirming incorporation. Cells were labeled without the addition of fosfomycin, indicating the HJH1 strain can use MurNAc-alk even when unmodified MurNAc is available in the cell.

Table 1. MurNAc-alk incorporation into PG

Muropeptide (non-reduced)	Theoretical Neutral Mass	MurNAc-alk labeled *H. pylori*			Control *H. pylori*		
		Observed Ion (charge)	Rt[1] (min)	Calculated Neutral Mass	Observed Ion (charge)	Rt[1] (min)	Calculated Neutral Mass
Di	696.270	697.289 (1+)	20.3	696.282	697.290 (1+)	20.4	696.283
Alk-Di	734.286	735.307 (1+)	30.5	734.300	-[2]	-	-
Tri	868.355	869.375 (1+)	15.8	868.368	869.374 (1+)	15.8	868.367
Alk-Tri	906.371	907.392 (1+)	25.8	906.385	-	-	-
Tetra	939.392	940.411 (1+)	20.4	939.404	940.412 (1+)	20.4	939.405
Alk-Tetra	977.408	978.428 (1+)	30.4	977.421	-	-	-
Penta	1010.429	1011.449 (1+)	22.9	1010.442	1011.449 (1+)	22.8	1010.442
Alk-Penta	1048.445	1049.464 (1+)	32.9	1048.457	-	-	-
TetraTri	1789.736	895.889 (2+)	33.4	1789.762	895.888 (2+)	33.3	1789.761
Alk-TetraTri	1827.752	914.898 (2+)	39.2	1827.781	-	-	-
TetraTetra	1860.774	931.407 (2+)	35.0	1860.799	931.407 (2+)	34.9	1860.799
Alk-TetraTetra	1898.789	950.416 (2+)	39.7	1898.817	-	-	-
TetraPenta	1931.811	966.926 (2+)	35.8	1931.837	966.925 (2+)	35.7	1931.835
Alk-TetraPenta	1969.826	985.934 (2+)	39.9	1969.853	-	-	-

[1] Rt, retention time.

[2] -, not detected.

Muropeptides detected (confirming incorporation) via LC-MS analysis of MurNAc-alk labeled versus control PG digests. (GM = GlcNAc-MurNAc). The control cells displayed no evidence of any MurNAc-alkyne incorporation.

As a second strategy for labeling new PG incorporation, we used D-alanine-alkyne (D-Ala-alk) (Kuru et al., 2012; Siegrist et al., 2013). This probe can be incorporated through the activity of PG transpeptidases (Figure 1 - supplement 1). To verify that D-Ala-alk is incorporated into the cell wall and to determine the position(s) at which it is incorporated, we purified sacculi from wild-type (LSH100) cells labeled for six doublings for analysis. D-Ala-alk was detected in only pentapeptide monomers and tetra-pentapeptide dimers, indicating that D-Ala-alk is exclusively incorporated at the pentapeptide position (Figure 4C and supplement 3).

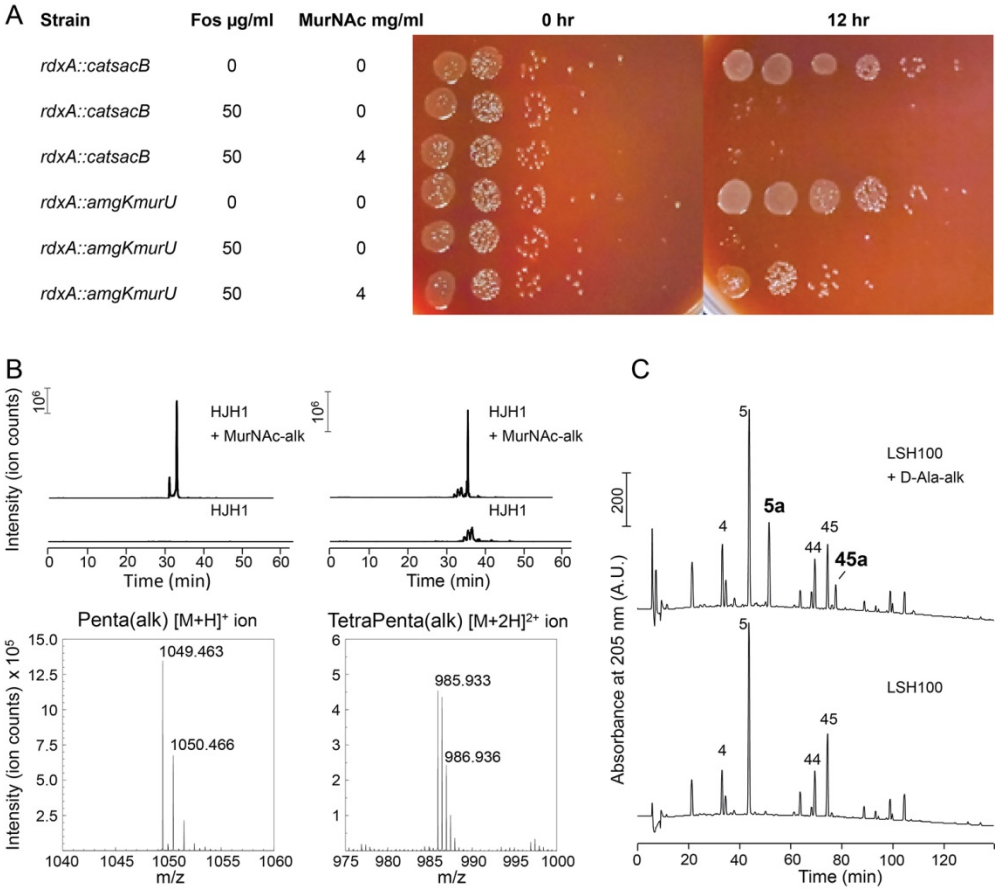

Figure 4. Validation of PG metabolic probes. (**A**) 10-fold dilutions showing LSH108 (*rdxA::catsacB*) or HJH1 (*rdxA::amgKmurU*) treated with 50 µg/ml fosfomycin and supplemented with 4 mg/ml MurNAc, from one representative of three experiments. (**B**) Verification of MurNAc-alk incorporation into pentapeptides (left column) and tetra-pentapeptides (right column) by HPLC/MS/MS. Upper traces show extracted ion chromatograms (EICs) for the ion masses over the HPLC elution for unlabeled (lower EIC) and labeled (top EIC) sacculi. Bottom traces show spectra of the ions observed during LC-MS for the MurNAc-alk pentapeptide (bottom left, non-reduced, predicted $[M+H]^+$ ion *m/z* = 1049.452) and MurNAc-alk tetra-pentapeptide dimer (bottom right, non-reduced, predicted $[M+2H]^{2+}$ ion *m/z* = 985.920). Data shown are from one experiment. (**C**) Verification of D-Ala-alk incorporation into pentapeptides and tetra-pentapeptides. HPLC chromatograms of labeled (top) and unlabeled (bottom) sacculi. The main monomeric and dimeric muropeptides are labeled (4, disaccharide tetrapeptide; 5, disaccharide pentapeptide; 44, bis-disacccharide tetratetrapeptide; 45, bis-disacharide tetrapentapeptide). D-Ala-alk-modified muropeptides (top, 5a and 45a) are present only in the sample from labeled cells and were confirmed by MS analysis of the collected peak fractions. 5a, alk-labeled disaccharide pentapeptide (neutral mass: 1036.448); 45a, alk-labelled bis-disaccharide tetrapentapeptide (neutral mass: 1959.852). Data shown are from one experiment.

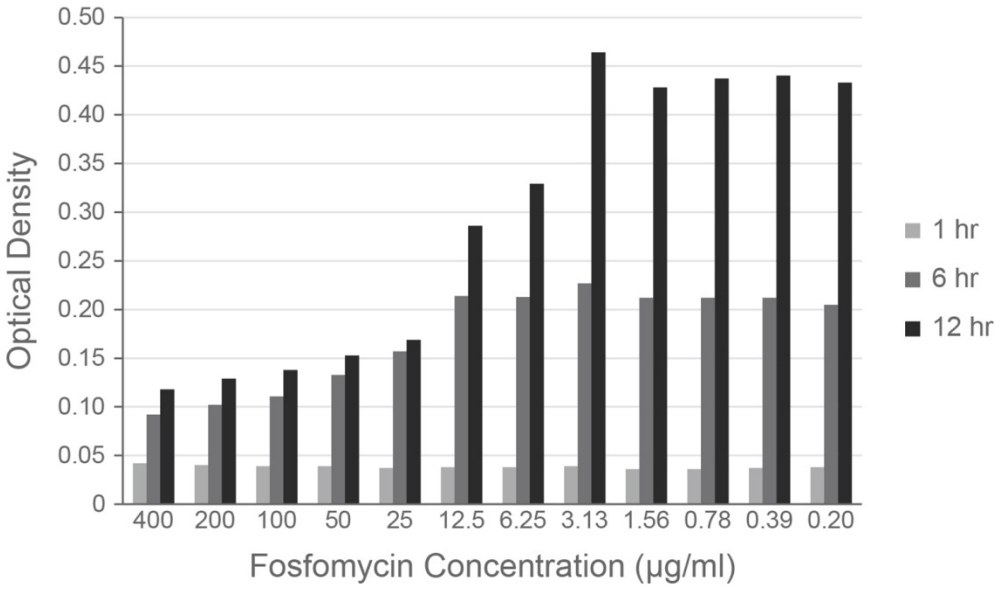

Figure 4 - figure supplement 1. The MIC of fosfomycin in *H. pylori* is 25 µg/ml. Optical density of wild-type *H. pylori* cultures grown in a 96-well plate with a 2-fold dilution series of fosfomycin. Optical density was measured at 1 (light gray), 6 (medium gray), and 12 (dark gray) hours of incubation. Figure shows one representative experiment of two.

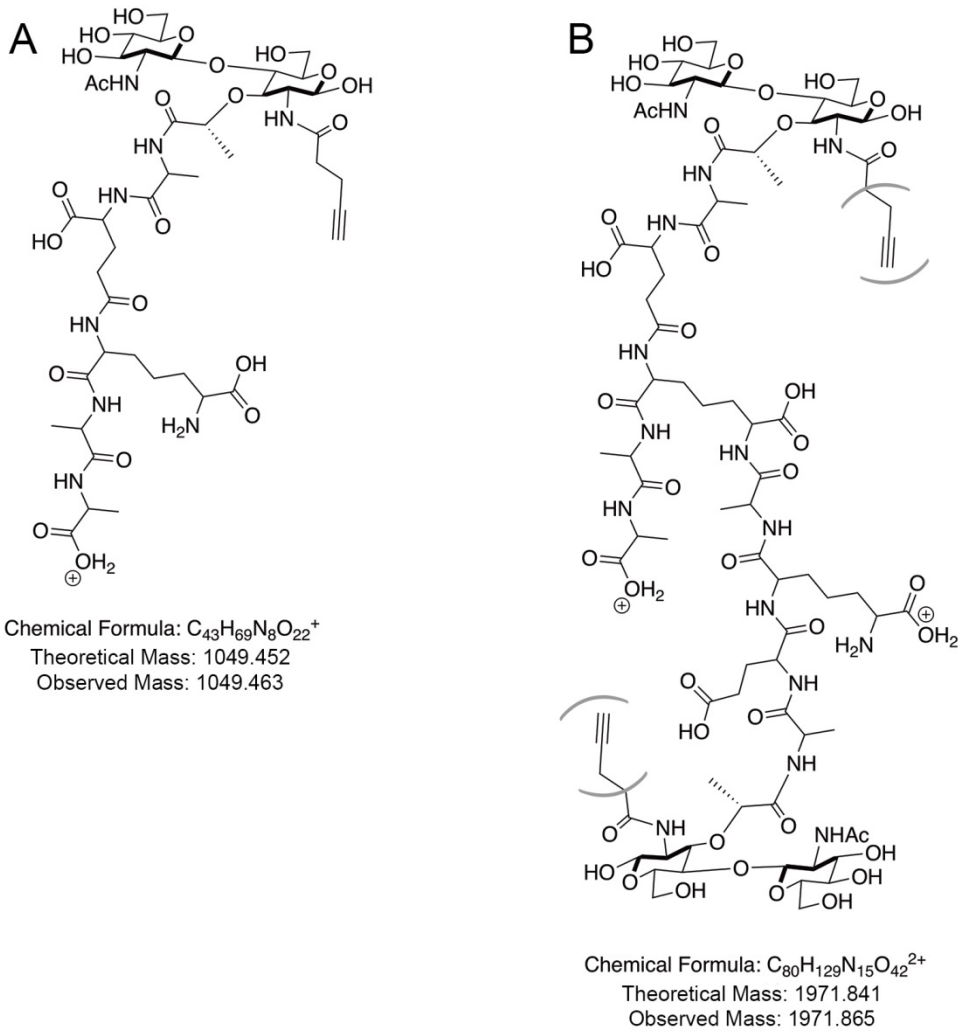

297

298 **Figure 4 - figure supplement 2. Detected MurNAc-alk labeled muropeptides.** Labeled (**A**) pentapeptide
299 monomer and (**B**) tetra-pentapeptide dimer ions. Parentheses indicate that the MurNAc-alk could be on
300 either the tetra or penta portion of the dimer; these two species are indistinguishable in our
301 HPLC/MS/MS data.

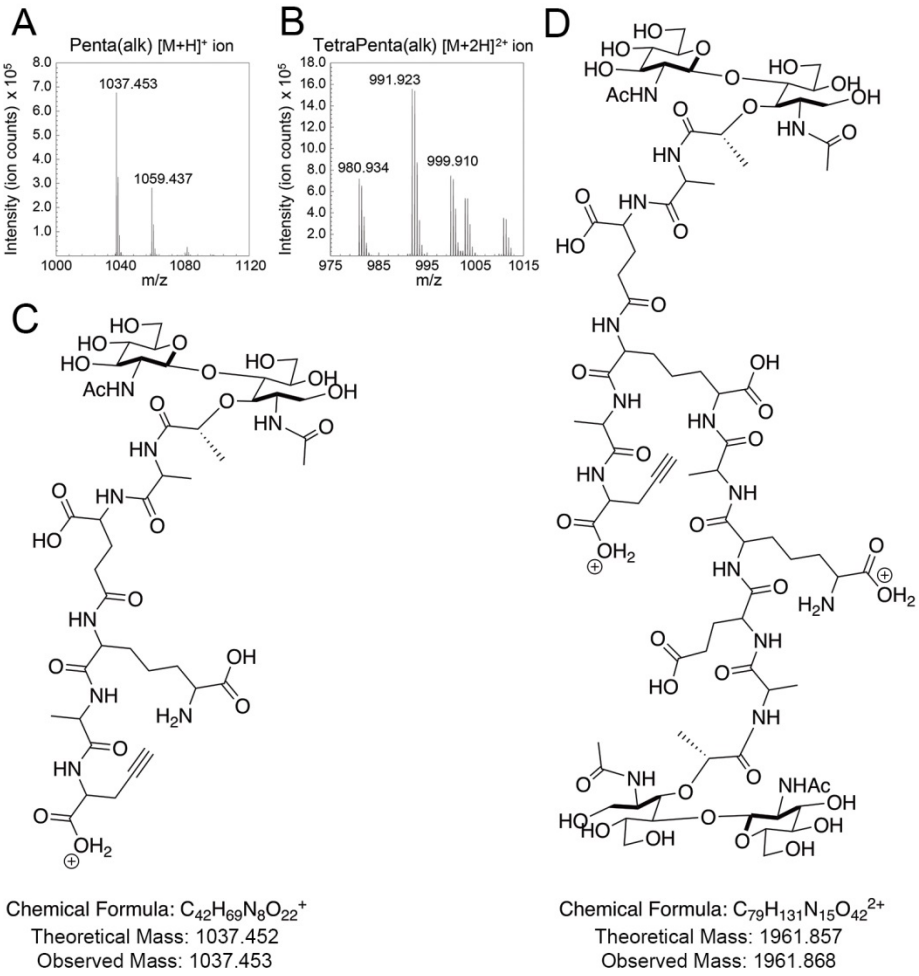

302

303 **Figure 4 - figure supplement 3. Detected D-Ala-alk labeled muropeptides.** Mass spectra for the ions
304 observed for the reduced (**A**) D-Ala-alk pentapeptides (left, Peak 5a in Figure 4C) and (**B**) D-Ala-alk tetra-
305 pentapeptides (right, Peak 45a in Figure 4C). The labeled peaks, from left to right are: (**A**) D-Ala-alk-
306 pentapeptide+H^+ and D-Ala-alk-pentapeptide+Na^+ and (B) D-Ala-alk-tetra-pentapeptide+$2H^{2+}$, D-Ala-alk-
307 tetra-pentapeptide+H^++Na^+, and D-Ala-alk-tetra-pentapeptide+H^++K^+. Schematic of (**C**) labeled
308 pentapeptide monomer and (**D**) labeled tetra-pentapeptide dimer ions.

PG synthesis is enriched at both negative Gaussian curvature and the major helical axis area

To visualize new PG incorporation, we labeled HJH1 with either MurNAc-alk or D-Ala-alk for 18 minutes (approximately 12% of the doubling time). AF555-azide was conjugated to the alkyne groups using click chemistry and cells were counterstained with WGA-AF488. Cells were imaged using 3D SIM (Figure 5 and supplement 1). As expected, labeling was seen on the boundary of the cell but not in the cytoplasmic area (Figure 5D and H). For both metabolic probes, PG synthesis appeared to be excluded from the poles, dispersed along the sidewall, and present at septa. However, D-Ala-alk septal labeling appeared much brighter compared to MurNAc-alk septal labeling, indicating at least some difference between incorporation and/or turnover of the two probes. To discover if this labeling difference is due to curvature-biased transpeptidation rates, we also attempted labeling with dimers D-alanine-D-alanine-alkyne and D-alanine-alkyne-D-alanine, which is presumably incorporated predominantly through PG precursor biosynthesis in the cytoplasm, but no signal was detected (data not shown) (Liechti et al., 2014).

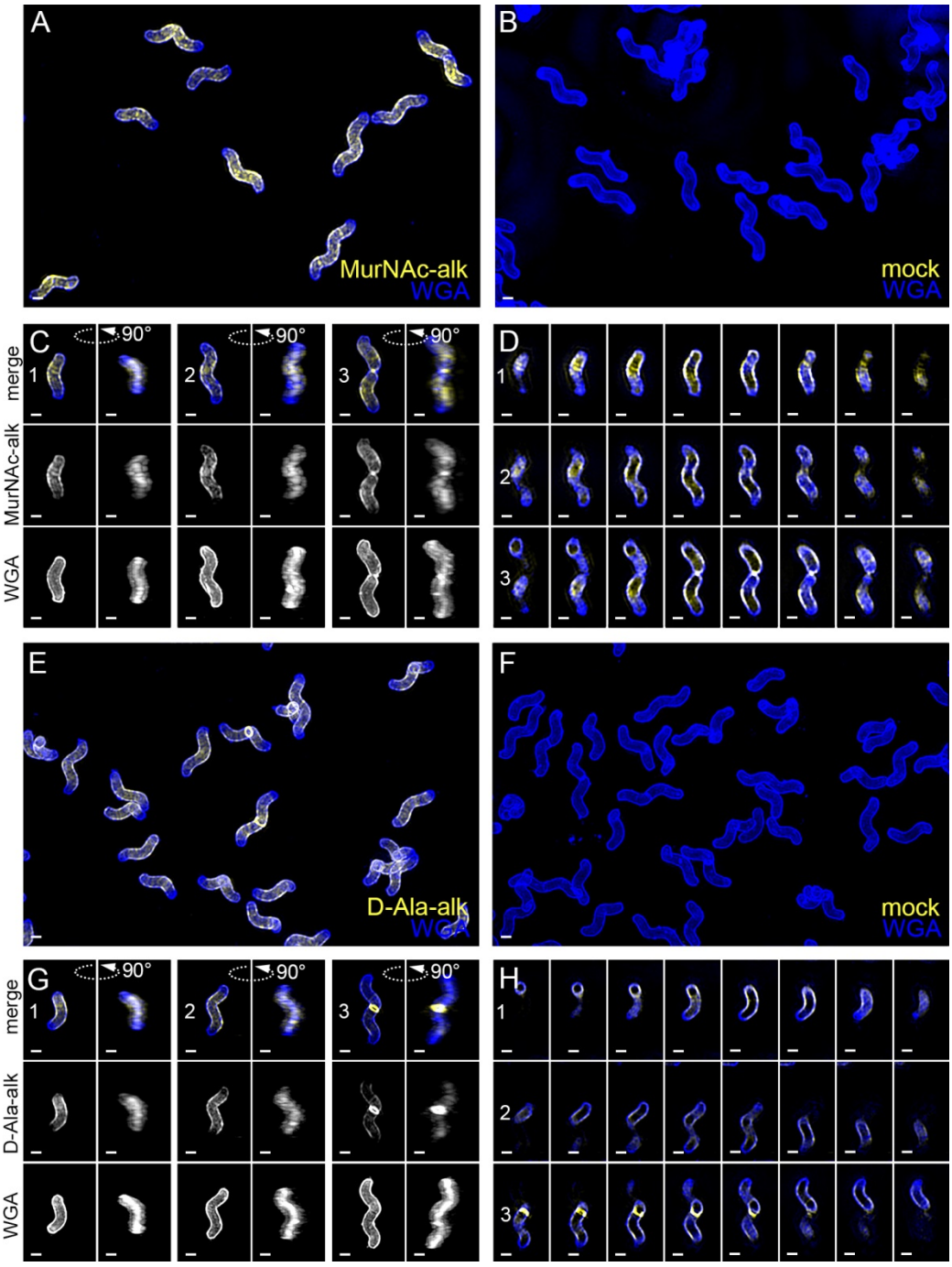

Figure 5. New cell wall growth appears dispersed along the sidewall, excluded from poles, and present at septa. 3D SIM imaging of wild-type cells labeled with an 18-minute pulse of MurNAc-alk (**A-D**, yellow) or 18-minute pulse of D-Ala-alk (**E-H**, yellow) counterstained with fluorescent WGA (blue). Color merged maximum projection of 18-minute MurNAc-alk (**A**), D-Ala-alk (**E**), or mock (**B**, **F**) labeling with fluorescent WGA counterstain. (**C**, **G**) Top-down (left) and 90-degree rotation (right) 3D views of three individual cells, including a dividing cell at the right. Top: color merge; middle: 18-minute MurNAc-alk (**C**) or D-Ala-alk (**G**); bottom: fluorescent WGA. (**D**, **H**) Color merged z-stack views of the three cells in C, G,

respectively (left to right = top to bottom of the cell). Numbering indicates matching cells. Scale bar = 1 µm. The represented images are selected from one of three biological replicates.

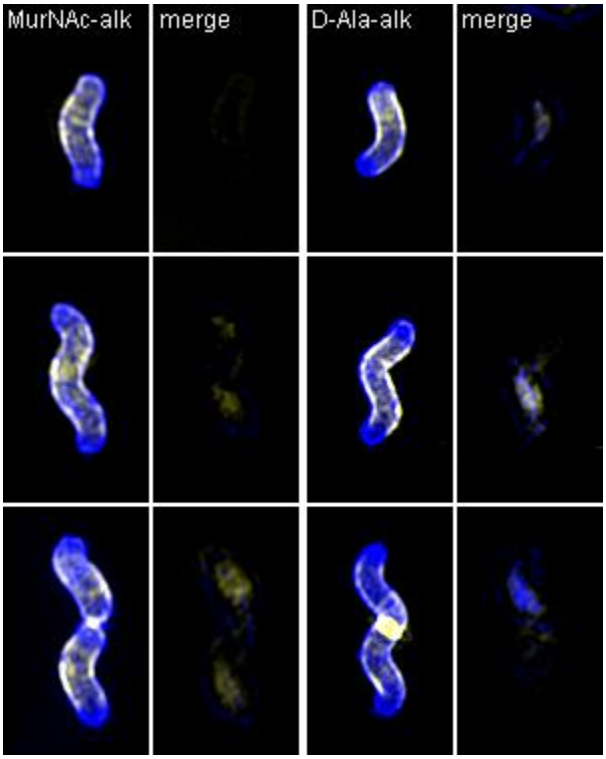

(placeholder for .avi)

Figure 5 - figure supplement 1. Volumetric rendering and z-slices of the example cells in Figure 5.

To quantify any curvature-based enrichment (expressed throughout as relative concentration vs. Gaussian curvature) of new cell wall synthesis, we used the fluorescent WGA signal to generate 3D cell surface reconstructions of hundreds of individual, non-septating cells labeled with MurNAc-alk, D-Ala-alk, or cells that were mock-labeled as a control. The Gaussian curvature was calculated at every location on the reconstructed 3D surface of the cell. Because the absolute amount of synthesis (or other signals of interest) can vary between cells, and because the level of illumination throughout the field of view is non-uniform, we set the average PG synthesis signal for each individual cell to one. We measured each cell's curvature-dependent PG synthesis signal intensity relative to that average value, normalized by the amount of that curvature present on the surface, since there is more surface area associated with positive Gaussian curvature than negative. We performed this analysis separately with the entire cell surface and with the sidewall only (poles removed). We then averaged the single cell measurements across more than 100 cells pooled from three biological replicates to obtain a profile of enrichment or depletion as a function of surface curvature. In these profiles, a relative concentration value of one indicates that the average PG synthesis signal intensity at that curvature is the same as the average across the cell surface. Values greater than one indicate curvatures where PG synthesis is enriched and values less than one indicate curvatures where PG synthesis is depleted.

Curvature enrichment analysis of whole cell surfaces revealed that for both metabolic probes, signal was largely absent from the poles, as seen by the drop-off of relative enrichment at curvatures above 10 μm^{-2} (Figure 6A). To focus on the curvature enrichment pattern along the sidewall, we repeated the analysis after first computationally removing the poles. Looking at sidewall curvature alone, MurNAc-alk was clearly enriched at two sites. At negative curvature, enrichment increases as curvature becomes more negative. At positive curvature, enrichment peaks near 6 μm^{-2} and then begins to decrease at higher curvatures (Figure 6B, green). D-Ala-alk showed peaks of enrichment aligning with those of MurNAc-alk (Figure 6B, blue), but the magnitude of the peak at positive curvature was reduced. The mock labeling control showed minimal curvature bias (Figure 6B, gray). This demonstrates that the fluorescent signal in the mock labeling is independent of geometry. Biological replicates were highly reproducible (Figure 6 - supplement 1).

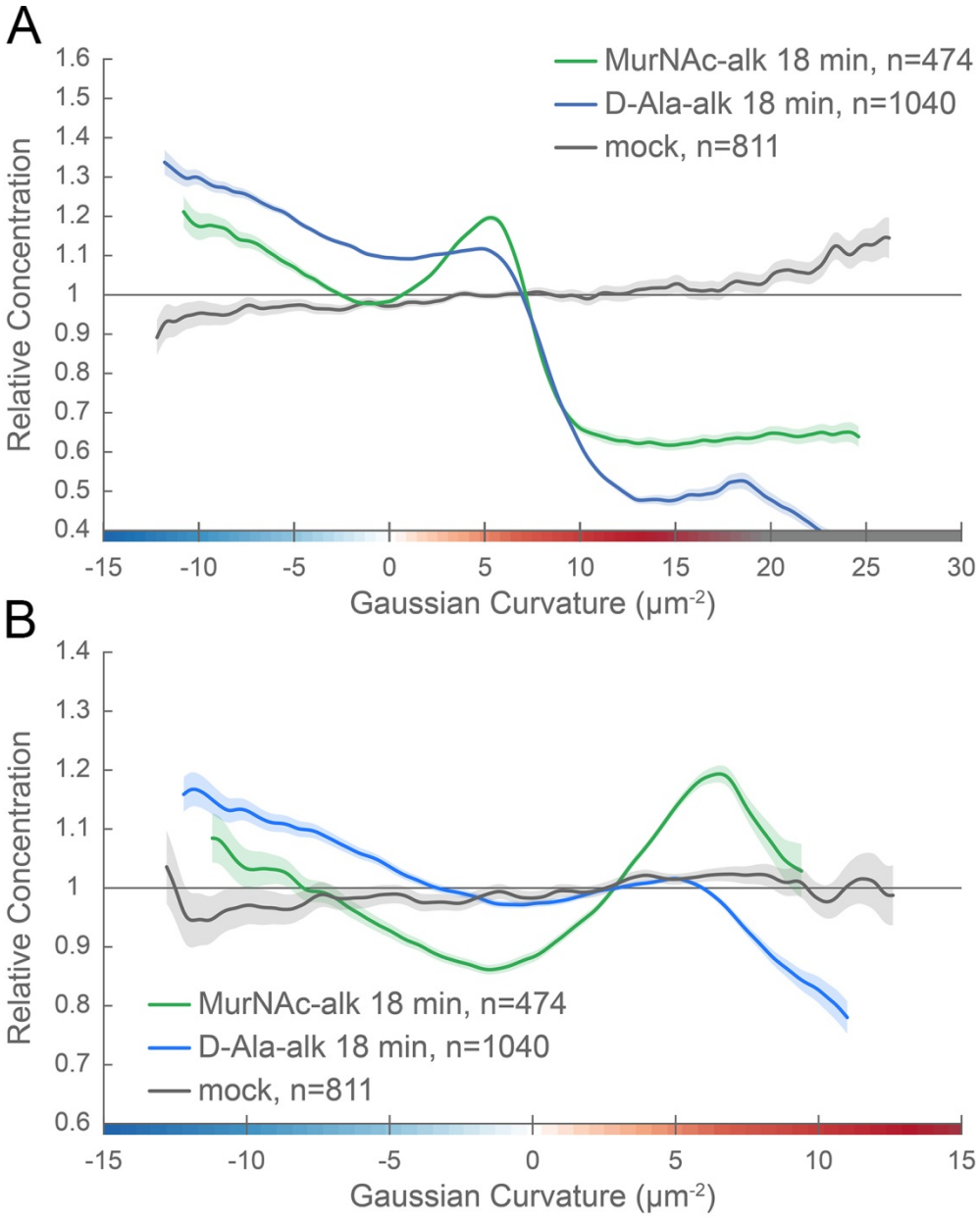

363

364 **Figure 6. New cell wall growth is excluded from the poles and enriched at negative Gaussian curvature**
365 **and the major axis area.** Whole surface (**A**) and sidewall only (**B**) surface Gaussian curvature enrichment
366 of relative concentration (>1 is enriched; <1 is depleted) of new cell wall growth (y-axis) vs. Gaussian
367 curvature (x-axis) derived from a population of computational cell surface reconstructions of MurNAc-
368 alk (green), D-Ala-alk (blue) 18-minute pulse-labeled, and mock-labeled (gray) cells. 90% bootstrap
369 confidence intervals are displayed as a shaded region about each line. The represented data are pooled
370 from three biological replicates.

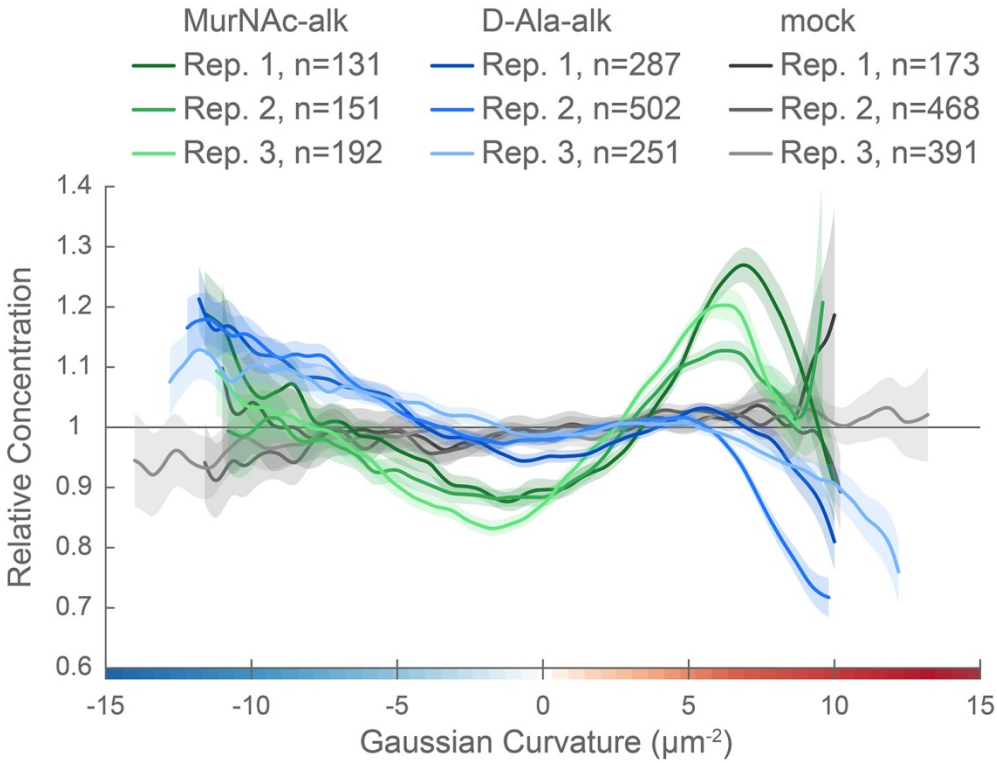

Figure 6 - figure supplement 1. Curvature preferences of MurNAc-alk-, D-Ala-alk-, and mock-labeling signal are highly reproducible. Sidewall only surface Gaussian curvature enrichment of relative concentration of new cell wall growth (y-axis) vs. Gaussian curvature (x-axis) of the three biological replicates pooled in Figure 6: MurNAc-alk (greens), D-Ala-alk (blues) 18-minute pulse-labeled, and mock-labeled (grays) cells. 90% bootstrap confidence intervals are displayed as a shaded region about each line.

MreB is enriched at negative Gaussian curvature

The cytoskeletal protein MreB has been shown in rod-shaped organisms to preferentially localize to negative Gaussian curvatures near to and below zero and help direct PG synthesis (Bratton et al., 2018; Ursell et al., 2014). We investigated MreB localization to determine if an altered curvature preference might account for the PG synthesis pattern we observed. Immunofluorescence labeling with 3D SIM imaging revealed that MreB is present at the cell periphery as many individual foci and some short arcs that appear to be oriented approximately circumferentially and excluded from the poles (Figure 7 and supplement 1). Only sparse foci were seen with immunofluorescence using the preimmune serum (Figure 7B). Curvature enrichment analysis of non-dividing cells confirmed that MreB localization is depleted at the poles (Figure 7 - supplement 2). Regardless of whether the poles were included in the

389 analysis, we observed as Gaussian curvature became more negative, relative MreB concentration
390 increased monotonically (Figure 7E and supplement 2). Biological replicates were highly reproducible
391 (Figure 7 - supplement 3). This echoes the enrichment of PG synthesis at negative Gaussian curvature; as
392 Gaussian curvature became more negative (below -2 μm^{-2}), relative PG synthesis increased
393 monotonically. Preimmune serum did not show a curvature preference (Figure 7E, gray). Thus, MreB
394 may promote the enhanced PG synthesis observed at negative curvature.

395

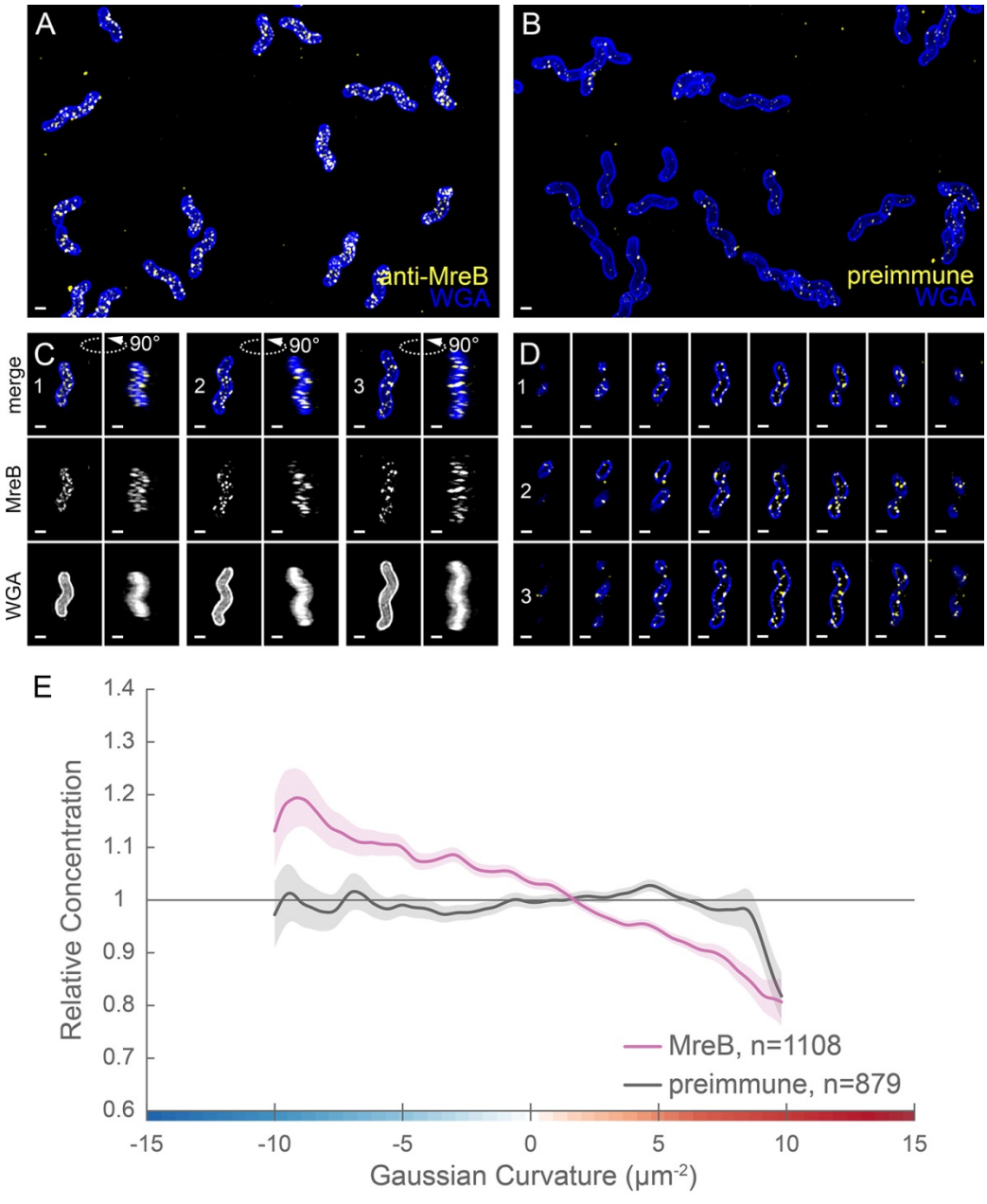

396

Figure 7. MreB is present as small foci enriched at negative Gaussian curvature. 3D SIM imaging of wild-type cells immunostained with anti-MreB (**A**, **C**, **D**, yellow) or preimmune serum (**B**, yellow) and counterstained with fluorescent WGA (blue). (**A**, **B**) Color merged maximum projections (**C**) Top-down (left) and 90-degree rotation (right) 3D views of three individual cells. Top: color merge; middle: anti-MreB; bottom: fluorescent WGA. (**D**) Color merged z-stack views of the three cells in A. (left to right = top to bottom of the cell). Numbering indicates matching cells. Scale bar = 1 µm. (**E**) Sidewall only surface Gaussian curvature enrichment plots for a population of cells immunostained with anti-MreB (pink), or pre-immune serum (gray). Smooth line plot (solid line) of relative MreB concentration (y-axis) vs. Gaussian curvature (x-axis) derived from a population of computational cell surface reconstructions with poles excluded. 90% bootstrap confidence intervals are displayed as a shaded region about each line. The represented images are selected from one of three biological replicates and the data are pooled from the three biological replicates.

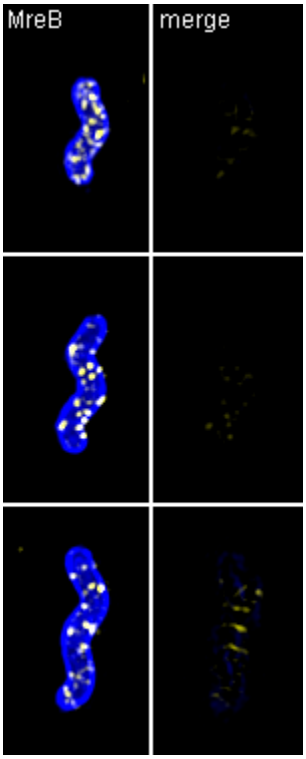

(placeholder for .avi)

Figure 7 - figure supplement 1. Volumetric rendering and z-slices of the example cells in Figure 7.

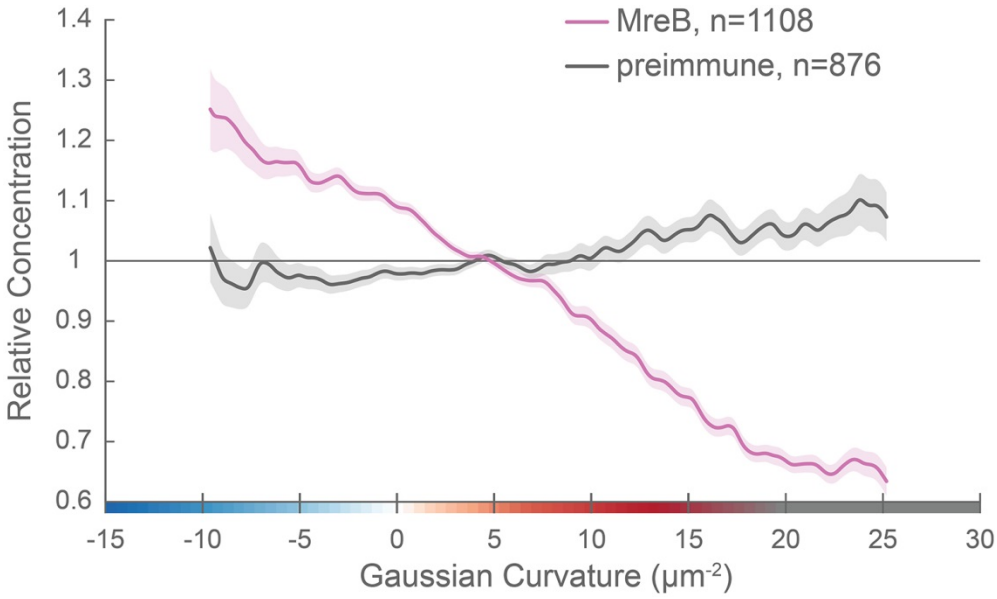

Figure 7 - figure supplement 2. MreB enrichment decreases with increasing positive Gaussian curvature. Whole surface (sidewall and poles) Gaussian curvature enrichment of relative MreB concentration (y-axis) vs. Gaussian curvature (x-axis) of computational cell surface reconstructions of a population of cells immunostained with anti-MreB (pink), or pre-immune serum (gray). 90% bootstrap confidence intervals are displayed as a shaded region about each line. The represented data are pooled from three biological replicates.

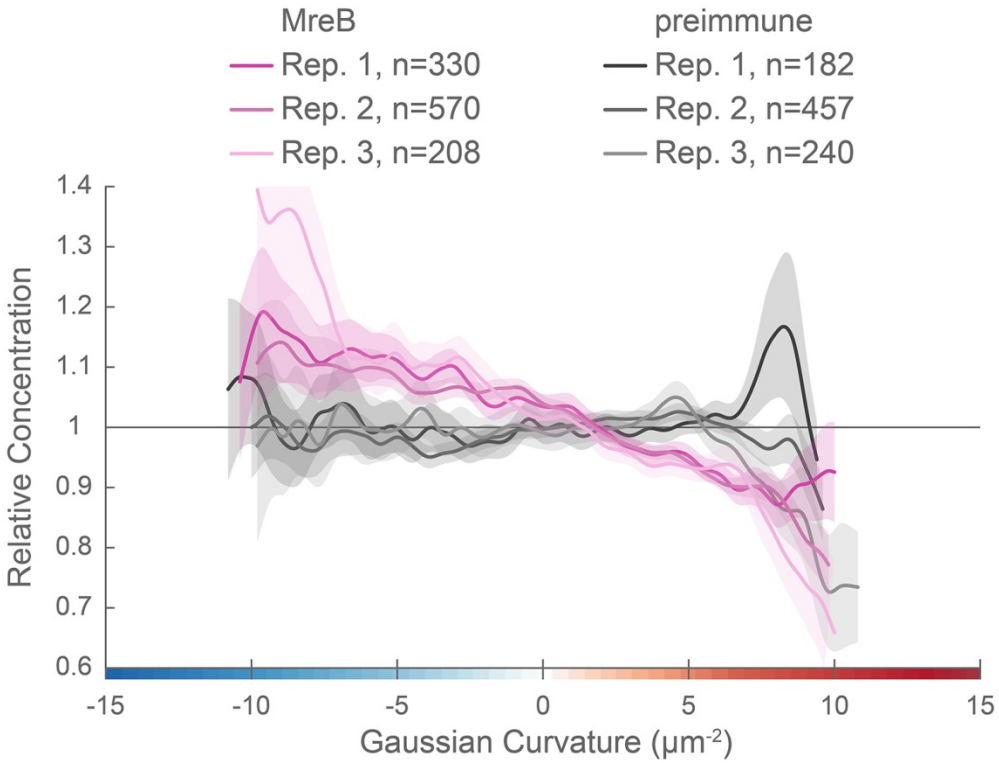

Figure 7 - figure supplement 3. Curvature preference of MreB is highly reproducible. Sidewall only surface Gaussian curvature enrichment of relative MreB concentration (y-axis) vs. Gaussian curvature (x-axis) of the three biological replicates pooled in Figure 7: anti-MreB (pinks) and preimmune serum (grays) immunostained cells. 90% bootstrap confidence intervals are displayed as a shaded region about each line.

The bactofilin CcmA forms filaments, bundles, and lattices *in vitro*

We reasoned that another cytoskeletal element might help boost PG synthesis at the major axis area. While both coiled-coil rich proteins (Ccrp) and the bactofilin homolog CcmA have been implicated in *H. pylori* cell shape (Specht et al., 2011; Sycuro et al., 2010; Waidner et al., 2009), only loss of CcmA, and not individual Ccrps, results in a drastic cell shape defect in our strain background; Δ*ccmA* cells are nearly straight. To verify CcmA's status as a cytoskeletal filament, we tested its ability to form higher-order structures *in vitro*. Negative staining of recombinant wild-type CcmA purified from *E. coli* revealed filaments of varying length, long helical bundles of filaments, and lattice structures (Figure 8A-B and supplement 1A). Fast Fourier transform analysis of the lattice structures revealed a filament spacing of 5.5 nm (Figure 8 - supplement 2), similar to that previously observed for *C. crescentus* BacA lattices (5.6

438 nm) (Vasa et al., 2015). While BacA forms orthogonal lattices, the CcmA lattices are skewed (acute angle
439 = 71.5°; obtuse angle = 106.2°).

440 To begin to assess the importance of higher-order structures and localization for CcmA cell shape
441 functions, we constructed two point mutant variant proteins, located in the predicted hydrophobic core
442 of the protein (I55A and L110S) (Shi et al., 2015). Homologous residues (75 and 130, respectively) were
443 shown to be important for polar localization of the bactofilin BacA in *C. crescentus* (Vasa et al., 2015).
444 While both proteins could be expressed and purified from *E. coli*, the recombinant proteins either fail to
445 form any higher order structures under any buffer condition tested (I55A; Figure 8C) or form no lattice
446 structures and many individual filaments in addition to bundles that are straighter, narrower, and
447 shorter than those of wild-type CcmA (L110S; Figure 8D and supplement 1B) *in vitro*. When expressed as
448 the sole copy of *ccmA* in *H. pylori*, both mutant proteins could be detected in whole cell extracts (Figure
449 8E), but the I55A variant showed lower steady-state protein levels than wild-type, while the L110S
450 variant consistently showed higher steady-state protein levels than wild-type. In both cases, the mutant
451 strains displayed a morphology indistinguishable from a *ccmA* null strain (Figure 8F and supplement 1C),
452 suggesting that formation of higher-order structures by CcmA may be necessary for cell shape-
453 determining functions.

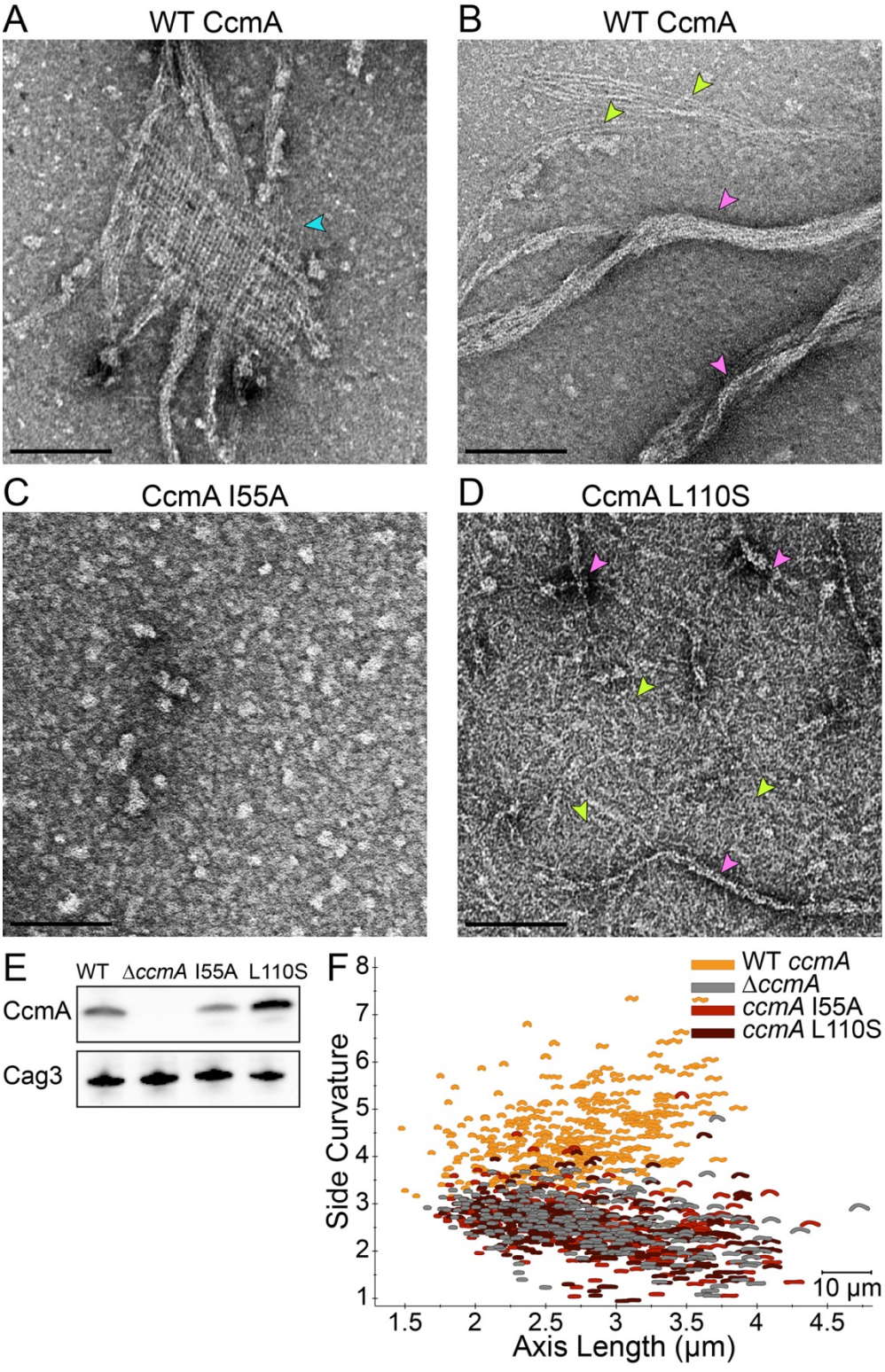

454

455 **Figure 8. Point mutations in CcmA cause altered polymerization *in vitro* and alter cell shape *in vivo*.** (**A-**
456 **D**) Negatively stained TEM images of purified CcmA. Scale bars = 100 nm, with representative images
457 from one of three experiments. Wild-type CcmA lattices (**A**, blue arrows) and helical bundles (**B**, pink

458 arrows), which are comprised of individual filaments (green arrows). (**C**) The I55A variant does not form
459 ordered structures *in vitro.* (**D**) CcmA^{L110S} filament bundles (pink arrows) and individual filaments (green
460 arrows). (**E**) Immunoblot detection of CcmA expression (top) in *H. pylori* lysates using Cag3 as loading
461 control (bottom); representative of four experiments. (**F**) Scatterplot displaying axis length (x-axis) and
462 side curvature (y-axis) of wild-type (gold), *ΔccmA* (gray), *ccmA*^{I55A} (red), and *ccmA*^{L110S} (dark red) strains.
463 Data are representative of two independent experiments. Wild-type, n=346; *ΔccmA*, n=279; *ccmA*^{I55A},
464 n=328; and *ccmA*^{L110S}, n=303.

465

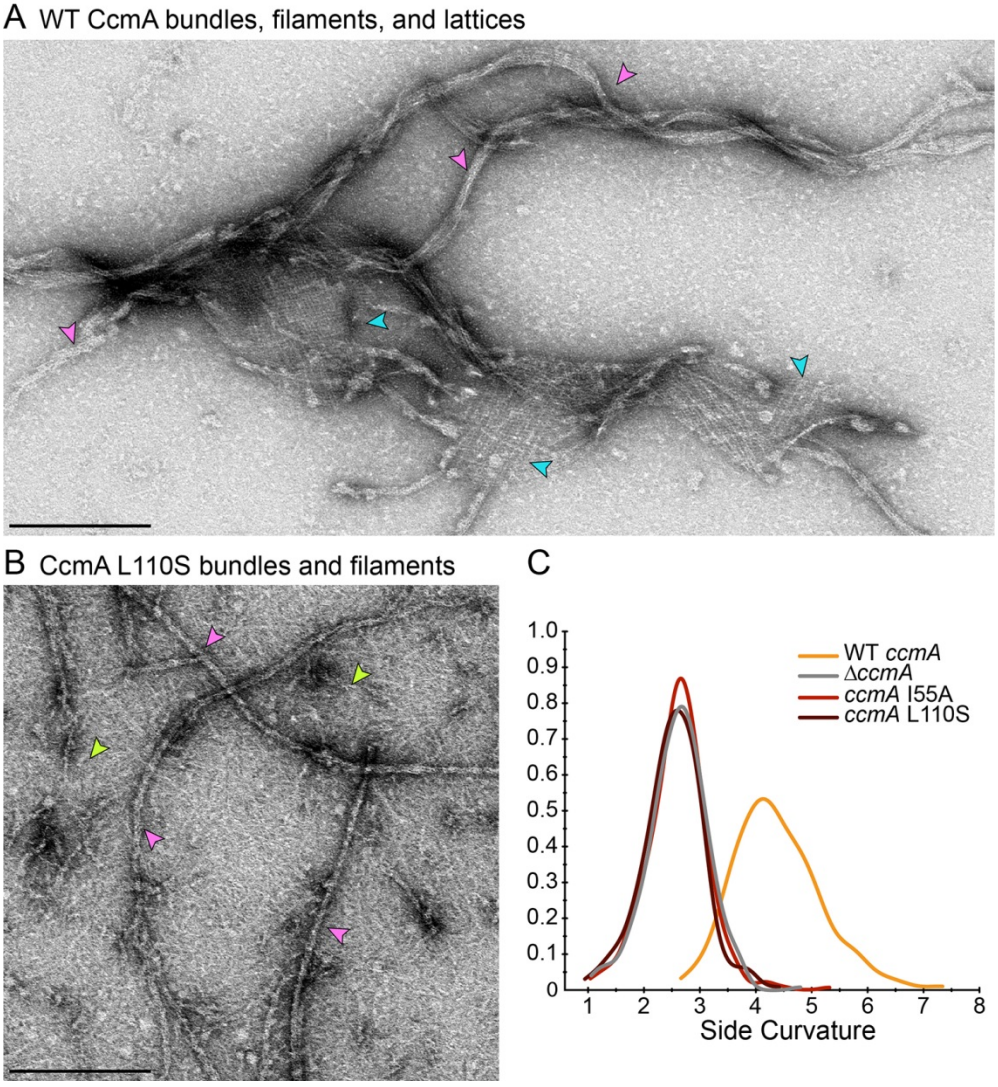

466

467 **Figure 8 - figure supplement 1. CcmA lattices and bundles.** Negatively stained TEM images of purified
468 CcmA. Scale bars= 200 nm. (**A**) Lower magnification view of wild-type CcmA, displaying both lattices
469 (blue arrows) and extended helical bundles (pink arrows). (**B**) Lower-magnification view of CcmA^{L110S},
470 displaying both individual filaments (green arrows) and bundles (pink arrows). (**C**) Smooth histogram of
471 population side curvature (x-axis) of cells in Figure 8F (one representative of two experiments).

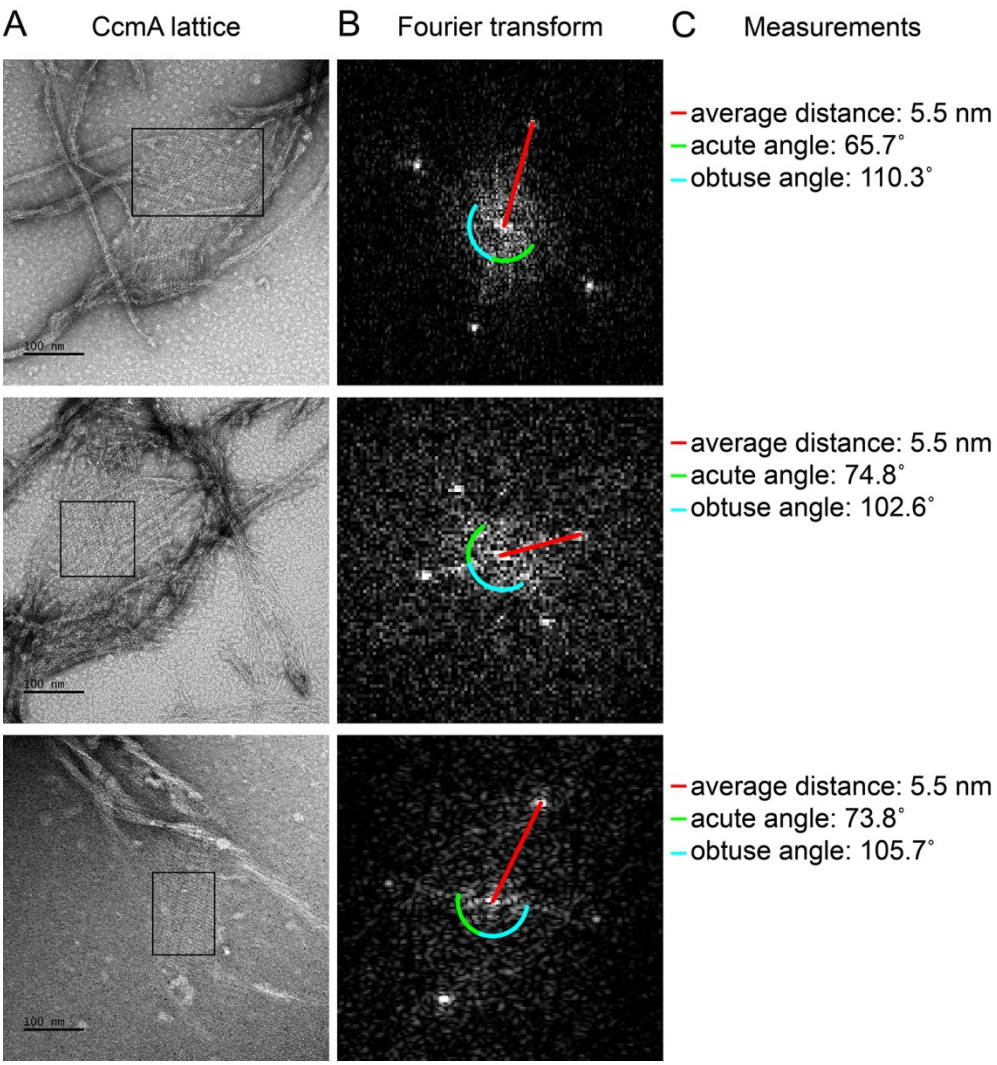

Figure 8 - figure supplement 2. Fourier transformation of CcmA lattices shows regular alignment and spacing. (**A**) Lattices formed from purified WT CcmA in 25 mM Tris pH 8. Scale bars = 100 nm. (**B**) Fast Fourier transform of the region inside each corresponding box in (**A**) performed using Fiji (Schindelin et al., 2012). After transformation, images were adjusted to enhance visualization (min: 134, gamma: 0.53, max: 172). (**C**) Average distance of bright spots from the center represents the distance between individual filaments in each lattice. Angle measurements between spots indicate the relative orientation of filaments within lattices. Average of the measurements from the three lattices: distance = 5.5 nm; acute angle = 71.5°; obtuse angle = 106.2°. Images shown are from one of three representative experiments.

CcmA localization to positive curvature correlates with cell wall synthesis, CcmA polymerization, and helical cell shape

To determine the subcellular localization of CcmA, we performed immunofluorescence of HJH1 cells expressing a 2X-FLAG epitope tag at the native locus under endogenous control as the sole copy of CcmA (Figure 9A and supplement 1). As shown previously (Blair et al., 2018), helical morphology is retained upon addition of the 2X-FLAG tag to the wild-type protein. Wild-type CcmA was observed at the cell boundary as puncta and short arcs and was largely absent from the center of the cell, indicating an association with the cell membrane (Figure 9D and supplement 1). Puncta were in some cases present as lines of dots roughly parallel to the helical (long) axis of the cell, but were also found distributed along the cell surface. Immunofluorescence was also performed on cells expressing wild-type or polymerization defective CcmA (CcmA I55A and L110S) using antisera raised against *H*. pylori CcmA (Figure 9 B, E-J and supplement 1). We detected some background signal in the interior of wild-type and mutant cells immunostained with CcmA preimmune serum, however signal was far stronger in cells immunostained with anti-CcmA (Figure 9 and supplement 2). In contrast to cells expressing the wild-type version of CcmA, the mutant CcmA proteins localized as puncta at the center with minimal signal at the cell boundary (Figure 9 G-J).

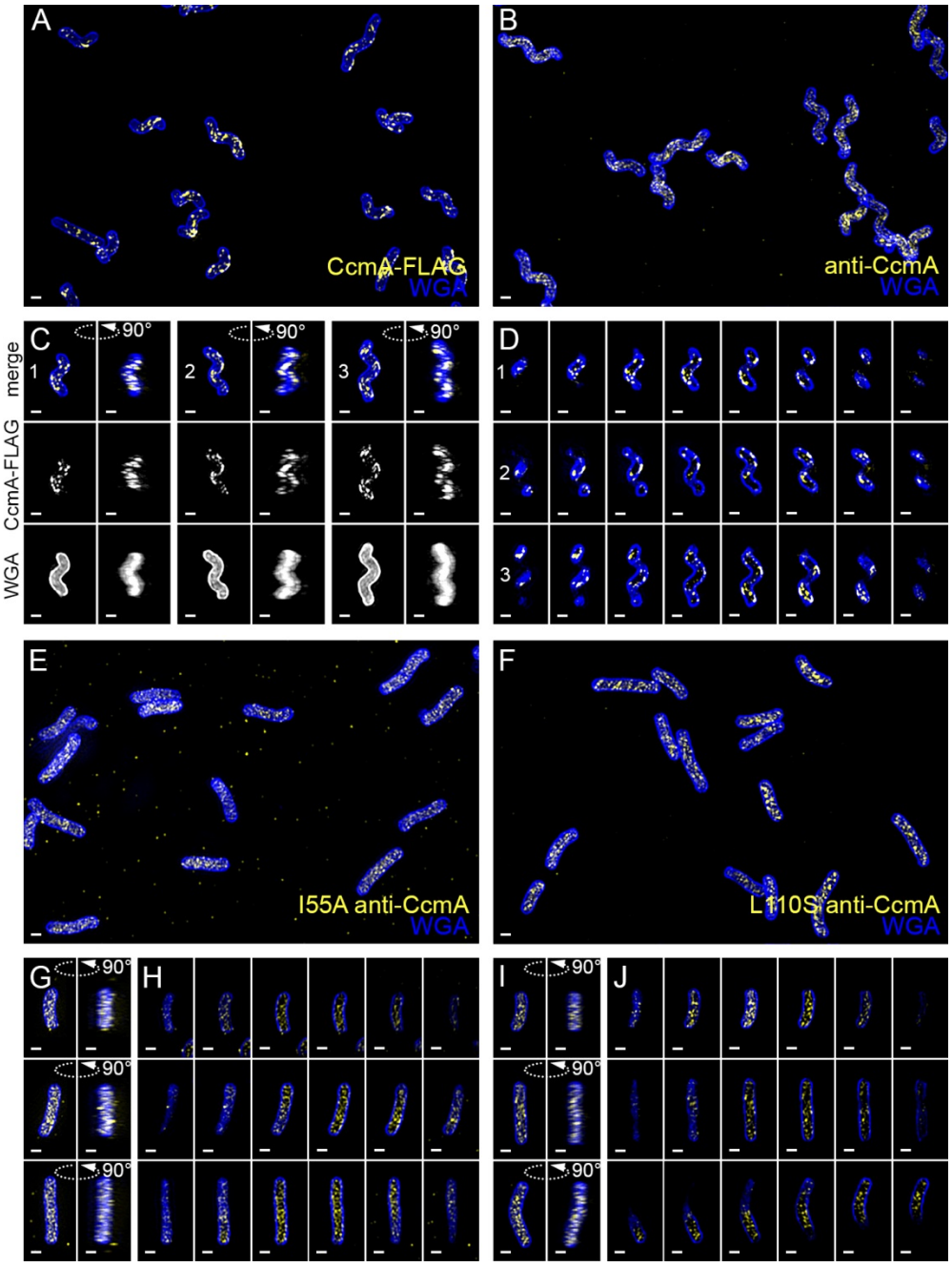

Figure 9. Wild-type CcmA appears as short foci on the side of the cell, but CcmA mutants I55A and L110S appear as foci in the interior of the cell. 3D SIM imaging of CcmA-FLAG cells immunostained with M2 anti-FLAG (**A**, **C**, **D**, yellow) or wild-type or CcmA point mutant cells immunostained with anti-CcmA (**B**, **E-H**, yellow); cells counterstained with fluorescent WGA (blue). (**A**) Color merged maximum projection of CcmA-FLAG immunostained with anti-FLAG and counterstained with fluorescent WGA. (**B**) Color merged field of view of wild-type cells immunostained with anti-CcmA and counterstained with fluorescent WGA. (**C**) Top-down (left) and 90-degree rotation (right) 3D views of three individual CcmA-FLAG cells. Top: color merge; middle: anti-FLAG; bottom: fluorescent WGA. (**D**) Color merged z-stack views of the three CcmA-FLAG cells in C. (left to right = top to bottom of the cell). Numbering indicates

matching cells. (**E**, **F**) Color merged field of view of I55A or L110S CcmA, respectively, immunostained with anti-CcmA and counterstained with fluorescent WGA. Top-down (left) and 90-degree rotation (right) 3D views of three individual I55A (**G**) or L110S (**I**) cells. (**H**, **J**) Color merged z-stack views of the three I55A cells in (**G**) or L110S cells in (**I**), respectively (Left to right = top to bottom of the cell). Scale bar = 1 µm. The represented images are selected from one of three biological replicates.

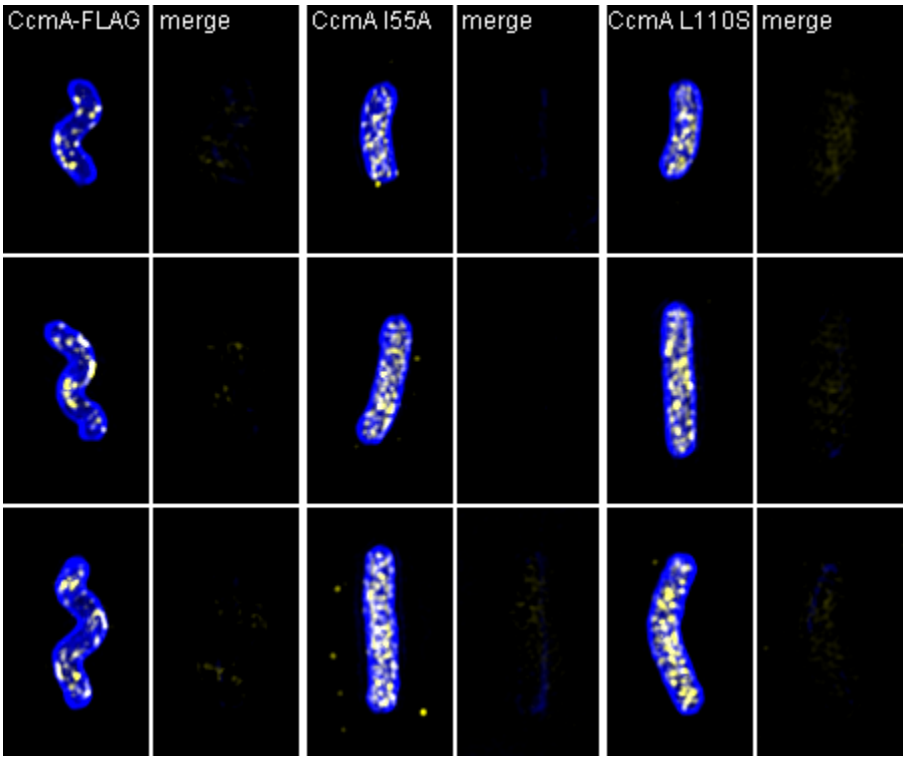

(placeholder for .avi)

Figure 9 - figure supplement 1. Volumetric rendering and z-slices of the example cells in Figure 9.

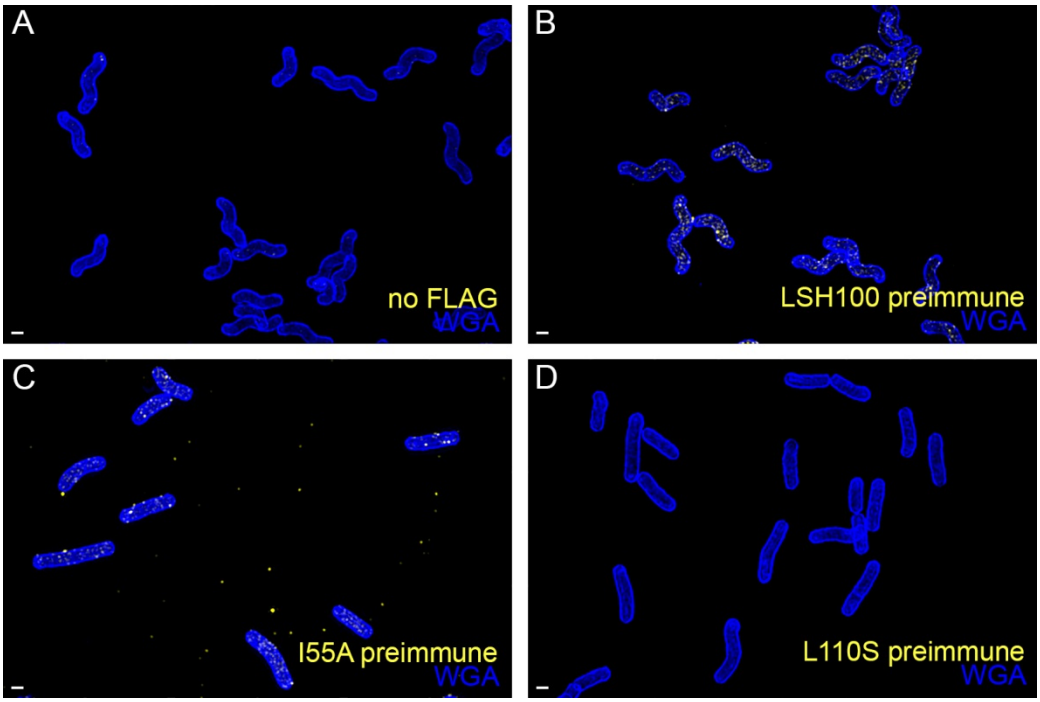

Figure 9 - supplement 2: There is minimal signal in the no-FLAG and preimmune serum controls. (**A**) Wild-type (no-FLAG) cells immunostained with M2 anti-FLAG (yellow) and counterstained with fluorescent WGA (blue). (**B**) wild-type, (**C**) I55A, or (**D**) L110S CcmA cells immunostained with CcmA preimmune serum (yellow) and counterstained with fluorescent WGA (blue). Scale bar = 1 µm. The represented images are selected from one of three biological replicates.

To determine if wild-type CcmA localization corresponds to the peak of PG synthesis at the major axis area, we performed curvature enrichment analysis of CcmA-2X-FLAG immunofluorescence images of non-dividing cells. CcmA was depleted at the poles (Figure 10 - supplement 1). With or without the poles, we saw a marked preference for the positive helical axis area (Figure 10A, red line and shaded box) that overlapped with the positive curvature enrichment peaks of MurNAc-alk and D-ala-alk (Figure 10A). The wild-type (no FLAG) negative control showed negligible curvature preference (Figure 10A and supplement 1) and biological replicates were highly reproducible (Figure 10 - supplement 2). We also performed curvature enrichment analysis on cells expressing wild-type, I55A, and L110S CcmA immunostained with anti-CcmA. Wild-type had a similar major axis area peak as CcmA-2X-FLAG (Figure 10, supplement 3, gold), with a lower magnitude due to a lower signal to noise ratio and an enrichment of background (preimmune) staining at negative Gaussian curvature (Figure 10 - supplement 3, gray). There was no distinguishable curvature preference for I55A or L110S CcmA compared to preimmune serum (Figure 10 - supplement 3, red and dark red, respectively), indicating that these proteins are

537 unable to localize preferentially to positive Gaussian surface curvature. These data suggest that proper
538 localization of CcmA to the major helical axis may be required for promoting cell wall synthesis at the
539 major axis area and patterning helical cell shape.

540

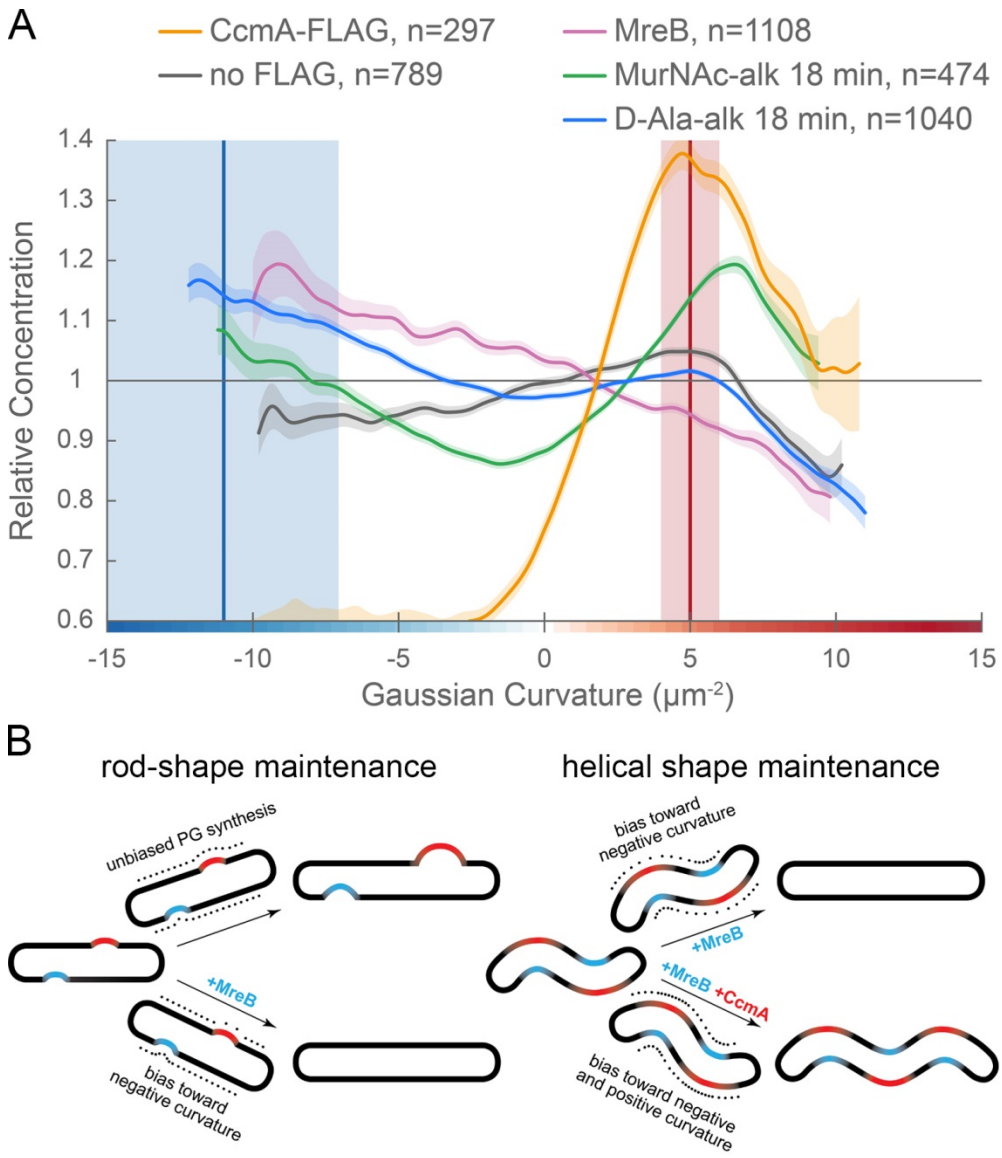

541

542 **Figure 10. CcmA curvature preference correlates with the peak of new PG incorporation at the major**
543 **axis area and MreB curvature preference correlates with new PG enrichment at negative Gaussian**
544 **curvature.** (**A**) Overlay of sidewall only surface Gaussian curvature enrichment of relative concentration
545 (y-axis) vs. Gaussian curvature (x-axis) from a population of computational cell surface reconstructions
546 with poles excluded of CcmA-FLAG (gold), no-FLAG control (gray), MreB (pink), MurNAc-alk (green), and
547 D-Ala-alk (blue). The represented data are pooled from three biological replicates. Blue and red vertical

548 lines and shaded regions indicate the average ±1 standard deviation Gaussian curvature at the minor
549 and major helical axis, respectively. (**B**) Model of the contribution of synthesis patterning to rod and
550 helical shape maintenance. Dots indicate different densities of cell wall synthesis that can decrease or
551 propagate non-zero Gaussian curvature. Colored shading indicates local regions of positive (red) and
552 negative (blue) Gaussian curvature.

553

554

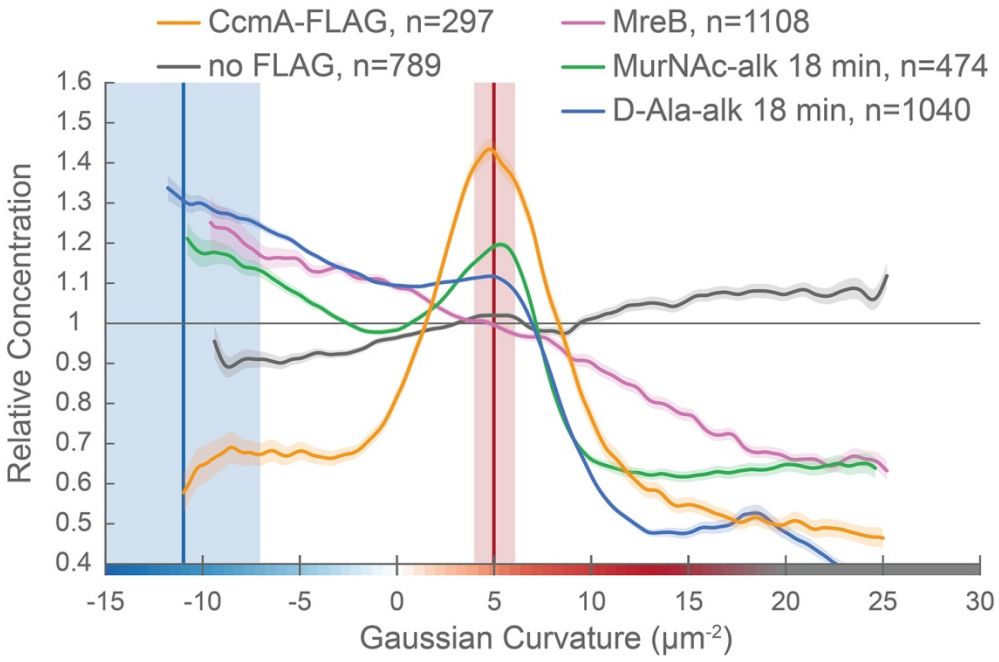

555

556 **Figure 10 - figure supplement 1. CcmA is excluded from the poles.** Whole surface (sidewall and poles)
557 Gaussian curvature enrichment of relative signal abundance (y-axis) vs. Gaussian curvature (x-axis)
558 derived from a population of computational cell surface reconstructions of CcmA-FLAG (gold), no-FLAG
559 (gray), MreB (pink), MurNAc-alk (green), and D-Ala-alk (blue). 90% bootstrap confidence intervals are
560 displayed as a shaded region about each line. The represented data are pooled from three biological
561 replicates. Blue and red vertical lines and shaded regions indicate the average ±1 standard deviation
562 Gaussian curvature at the minor and major helical axis, respectively.

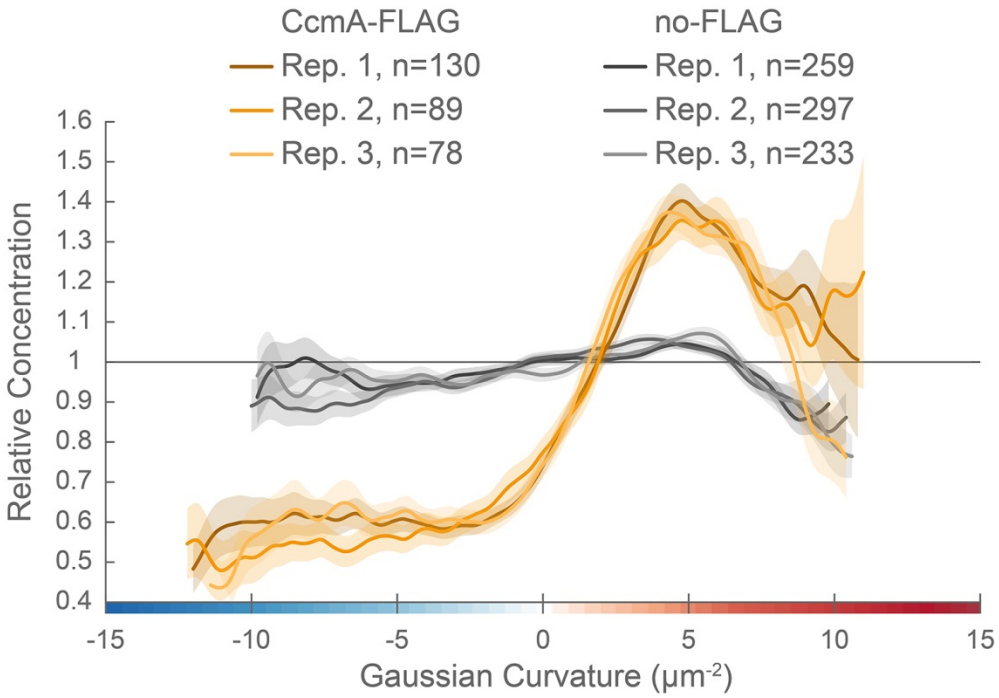

Figure 10 - figure supplement 2. Curvature preference of CcmA-FLAG is highly reproducible. Sidewall only surface Gaussian curvature enrichment of relative signal abundance (y-axis) vs. Gaussian curvature (x-axis) of the three biological replicates pooled in Figure 10: CcmA-FLAG (golds) and no-FLAG (grays) cells. 90% bootstrap confidence intervals are displayed as a shaded region about each line.

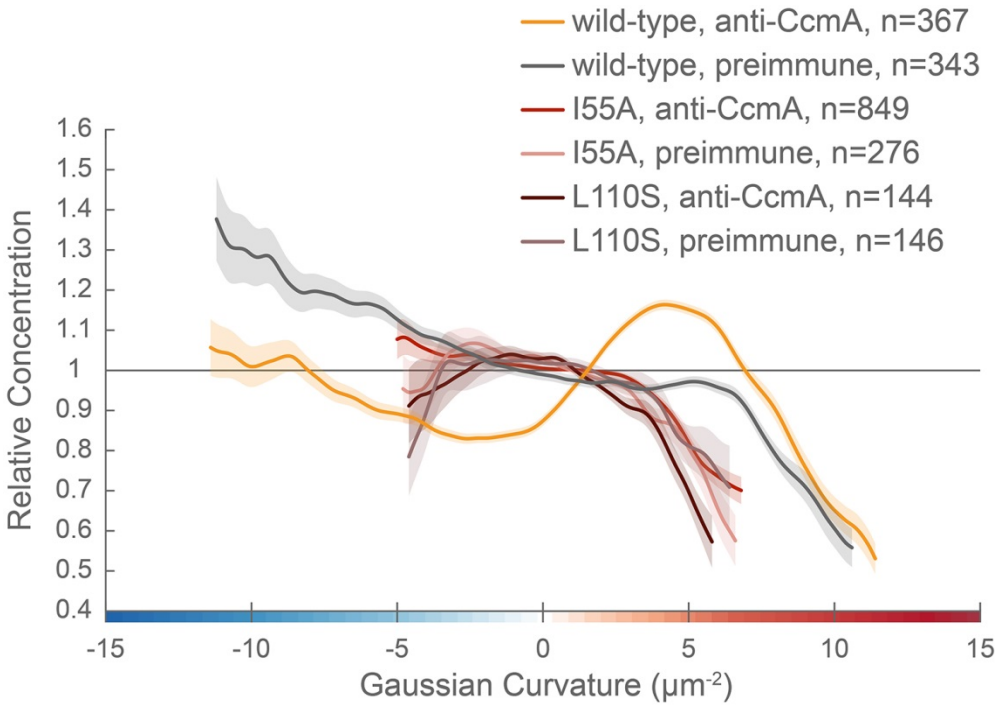

Figure 10 - figure supplement 3. CcmA mutants are not enriched at positive Gaussian curvature. Sidewall Gaussian curvature enrichment of relative signal abundance (y-axis) vs. Gaussian curvature (x-axis) for a population of computational cell surface reconstructions with poles excluded of wild-type LSH100 cells immunostained with anti-CcmA (gold) or preimmune serum (gray); CcmA I55A cells immunostained with anti-CcmA (red) or preimmune serum (light pink); or CcmA L110S cells immunostained with anti-CcmA (dark red) or preimmune serum (mauve). 90% bootstrap confidence intervals are displayed as a shaded region about each line.

Discussion

Bacterial cell shape is driven by patterning the cell wall. Maintenance of a cylindrical rod form in a variety of bacteria relies on the action of the actin-like protein MreB, which recruits PG synthesis along the sidewall (Typas et al., 2012; Zhao et al., 2017). Detailed analysis of MreB localization in the Gram-negative straight-rod *E. coli* indicates that centerline straightness and diameter uniformity rely on MreB curvature enrichment (Bratton et al., 2018; Ursell et al., 2014). MreB localization and thus cell wall synthesis are enhanced at cell wall dimples (negative Gaussian curvature), cylindrical regions (zero Gaussian curvature), and limited at cell wall bulges (positive Gaussian curvature). This pattern minimizes local curvature as growth progresses (Figure 10B, left). While such a growth pattern is at odds with maintaining areas of negative and positive Gaussian curvature required for curved- and helical-rod shapes, MreB is present in many bacteria with these shapes. The curved-rod shaped Gram-negative Proteobacteria *Caulobacter crescentus* and *Vibrio cholerae* appear to limit PG synthesis at negative curvatures through the action of long, cell-spanning cytoskeletal filaments (CreS and CrvA) that preferentially localize to the minor axis (negative Gaussian curvature) and enable cells to increase relative synthesis rates on the opposite side of the wall (positive Gaussian curvature) (Bartlett et al., 2017; Cabeen et al., 2009). We propose that the helical Proteobacterium *H. pylori* uses different mechanisms than *C. crescentus* and *V. cholerae* to maintain the even higher levels of negative and positive Gaussian curvature required for its helical cell shape; *H. pylori* leverages the bactofilin CcmA, which localizes preferentially to the major helical axis area, to promote synthesis at positive Gaussian curvatures on the sidewall, counterbalancing the MreB-driven enhanced synthesis at negative Gaussian curvatures (the minor helical axis) (Figure 10B, right).

To probe cell wall synthesis patterns in *H. pylori*, we used distinct metabolic probes to label the sugar (MurNAc-alk) and peptide (D-Ala-alk) portions of the polymer. While both probes indicate enhanced synthesis at the major and minor helical axes relative to the rest of the sidewall, there were considerable differences in enrichment peak magnitudes between the MurNAc-alk and D-Ala-alk probes. Modified D-alanine is thought to be incorporated into the cell wall through the action of synthesis-associated D-D-transpeptidases and cell wall-modifying L-D-transpeptidases, potentially complicating interpretation of this label. *H. pylori* does not have any known functional L-D-transpeptidases and no detectable 3-3 crosslinks, a hallmark of L-D-transpeptidase activity (Costa et al., 1999; Sycuro et al., 2010). Thus, signal from D-Ala-alk likely reports on D-D-transpeptidase activity. It is possible that D-D-transpeptidation may also occur separately from synthesis to promote cell wall remodeling or that the

608 rates of synthesis-associated transpeptidation activity may vary on different sides of the cell. We only
609 observed D-Ala-alk incorporation at the penta position (Figure 4B). *H. pylori* has a pentapeptide-rich cell
610 wall and it is unclear if *H pylori* actively regulates pentapeptide trimming. However, the cell shape
611 determining protein Csd3/HdpA has been shown to have weak pentapeptide carboxypeptidase activity
612 *in vitro* (Bonis et al., 2010). Pentapeptides can also be trimmed via transpeptidase-mediated hydrolysis
613 (Ghuysen, 1991). Curvature-biased trimming by either mechanism could also contribute to the
614 difference between the D-Ala-alk and MurNAc-alk curvature enrichment. The MurNAc probes have none
615 of these complications as they are embedded in the glycan.

616 We provide the first example of MreB curvature enrichment analysis in a curved- or helical-rod
617 bacterium and show that preference for negative Gaussian curvature is retained, even across the broad
618 range of curvatures represented on the *H. pylori* sidewall. While there has been report of MreB being
619 non-essential in *H. pylori* (Waidner et al., 2009), we have been unsuccessful in making a deletion mutant
620 (data not shown), suggesting that MreB is functional and important in *H. pylori*. We propose that MreB
621 promotes the peak of PG synthesis we observed at negative Gaussian curvature given its preference for
622 this curvature in *H. pylori* and its role in localizing PG synthesis activity in other organisms. To enable
623 maintenance of high sidewall curvature in the presence of the MreB-driven straight-rod cell growth
624 pattern, we suggest that *H. pylori* augments the default rod pattern by means of enhanced growth at
625 the major axis area that is independent of MreB (Figure 10B).

626 A major outstanding question is how *H. pylori* enhances PG synthesis activity at the major axis area. Our
627 3D analysis establishes that the average Gaussian curvature along the major axis is distinct from that
628 along the minor axis (5 vs. -11 μm^{-2}, respectively) and that the major axis is on average 70% longer than
629 the minor axis in the strain used here. Cytoskeletal elements can form higher-order structures that
630 reach a sufficient size scale to be able to sense surface curvature, providing a potential mechanism for
631 targeting synthesis to a specific range of positive Gaussian curvature. The bactofilin CcmA is the only
632 non-essential cytoskeletal protein we have identified in our strain background that makes an
633 indispensable and non-redundant contribution to helical shape maintenance. In contrast to the cell
634 spanning filaments CreS and CrvA, which reside at the minor axis, we show that CcmA is present in cells
635 as numerous puncta that have a preference for the major axis area. We propose that CcmA acts to
636 enhance synthesis on its preferred cell face by promoting PG synthesis locally (at positive Gaussian
637 curvature). In support of this hypothesis, the bactofilins BacA and BacB in *Caulobacter crescentus* recruit
638 the PG synthase PBPC to assist in stalk elongation, indicating that they help recruit PG synthesis (Kühn et

al., 2010). Additionally, our group recently showed that CcmA co-purifies with Csd5 and MurF, an enzyme involved in PG precursor synthesis (Blair et al., 2018), and separately that both CcmA and MurF are within the top 20 mass spec hits of a Csd7 immunoprecipitation (Yang et al., 2019, in revision). It is possible that CcmA may also help promote localized crosslink trimming, as loss of CcmA results in an increased degree of crosslinking in the sacculus (Sycuro et al., 2010). Crosslink trimming may help promote synthesis but could also play some other role in helical shape maintenance. CcmA dynamics could also influence its ability to promote cell shape. In other organisms, MreB filaments travel in a roughly circumferential path around the cell and we expect MreB to behave similarly in *H. pylori*. CcmA, however, does not require a nucleotide cofactor for polymerization, and thus may not be highly mobile unless coupled with the motion of PG synthesis machinery.

Loss of CcmA results in cells with highly diminished cell curvature and without significant helical twist. Beyond helping promote curvature by localized PG synthesis, it is possible that CcmA also helps generate twist. We observed helical bundles of filaments *in vitro* by TEM. These bundles are far longer than the foci we see by immunofluorescence, but foci within the cell may consist of short twisted filament bundles and/or skewed lattices. While it remains unclear how filament or lattice twist would be coupled to cell wall twist, a recently-published paper demonstrated that the bactofilin LbbD modulates helical pitch in the spirochete *Leptospira biflexa* (Jackson et al., 2018). Both CcmA point mutant variants show altered or no polymerized structures under a variety of buffer conditions *in vitro* and fail to localize to the cell envelope *in vivo*. It is still unclear which structures are relevant and if altering higher-order structures abolishes CcmA function by disrupting protein-protein interactions and/or CcmA localization.

Overall, our results are consistent with a model in which MreB-patterned straight-rod shape is the default pattern for *H. pylori* cells and helical shape is achieved by adding major axis area PG synthesis via CcmA to augment straight-rod cell wall patterning. The enrichment of new cell wall synthesis to both negative Gaussian curvature, as expected for straight-rod shape, and to the major axis area indicates one mechanism for achieving helical shape, but it is not apparent how this growth pattern on its own could be sufficient for helical shape maintenance. The low amount of synthesis at Gaussian curvatures corresponding to the sides of the cell body in comparison to the major and minor axis areas is both unexpected and counterintuitive; it suggests additional mechanisms may be required to maintain helical shape. Indeed, the noted difference between enrichment of D-Ala-alk and MurNAc-alk suggests that spatially-coordinated cell wall modification occurs. Curvature-dependent differences in crosslinking could alter cell wall mechanical properties and PG density; perhaps the PG at the side of the cell is less

dense, thus requiring less PG synthesis during growth. Furthermore, our labeling strategy allowed us to determine the curvature bias of new PG insertion, but this insertion may be counterbalanced by spatially-regulated turnover of old PG. We also do not know if super-twisting of the cell wall occurs during growth: does PG on the major axis remain at the major axis as the cell grows?

We employed sophisticated computational tools to demonstrate that *H. pylori* must achieve a much broader distribution of sidewall Gaussian curvature than the curved-rod bacteria *C. crescentus* and *V. cholerae* and that it uses distinct mechanisms to achieve these curvatures. In elucidating the spatial patterning of new cell wall synthesis, we have revealed one of the downstream mechanisms of *H. pylori*'s cell shape-determining program.

Materials and Methods

Cultures and growth

H. pylori (LSH100 and derivatives, Table 2) was grown on horse blood (HB) agar plates (Humbert and Salama, 2008) incubated at 37°C under micro-aerobic conditions in either 90% air, 10% CO_2 (dual-gas) or in 10% CO_2, 10% O_2, 80% N_2 (tri-gas). For resistance marker selection, HB agar plates were supplemented with 15 µg/ml chloramphenicol, 25 µg/ml kanamycin, or 30 mg/ml sucrose, as appropriate. Liquid *H. pylori* cultures were grown shaking in Brucella broth (BD Biosciences, Sparks, MD) supplemented with 10% heat-inactivated fetal bovine serum (Gemini Bio-Products, West Sacramento, CA) (BB10) at 37°C in tri-gas conditions. For plasmid selection and maintenance, *E. coli* cultures were grown in lysogeny broth (LB) or agar supplemented with 100 µg/ml ampicillin at 37°C.

Table 2. Strains used in this study

Strain	Genotype/description	Construction	Reference
LSH100	Wild-type: mouse-adapted G27 derivative	-	Lowenthal et al., 2009
LSH141 (*Δcsd2*)	LSH100 *csd2::cat*	-	Sycuro et al., 2010
TSH17 (*Δcsd6*)	LSH100 *csd6::cat*	-	Sycuro et al., 2013
LSH108	LSH100 *rdxA::aphA3sacB*	-	Sycuro et al., 2010
HMJ_Ec_pLC292-KU	*E. coli* TOP10 pLC292-KU	Transformation of TOP10 with pLC292-KU	This study
HJH1	LSH100 *rdxA::amgKmurU*	Integration of pLC292-KU into LSH108	This study
JTH3	LSH100 *ccmA:2X-FLAG:aphA3*	-	Blair et al., 2018
JTH5	LSH100 *ccmA:2X-FLAG:aphA3 rdxA::amgKmurU*	Natural transformation of HJH1 with JTH3 genomic DNA	This study
KGH10	NSH57 *ccmA::catsacB*	-	Sycuro et al., 2010
LSH117	LSH100 *ccmA::catsacB*	Natural transformation of LSH100 with KGH10 genomic DNA	This study
SSH1	LSH100 *ccmA*^{I55A}	Natural transformation with *ccmA I55A* PCR product	This study
SSH2	LSH100 *ccmA*^{L110S}	Natural transformation with *ccmA L110S* PCR product	This study

Constructing AmgK MurU strain

AmgK and MurU-encoding sequences were PCR amplified from expression plasmid pBBR-KU (Liang et al., 2017) using primers AmgK_BamHI_F and MurU_HindIII_R (Table 3). The AmgK MurU amplification product and plasmid pLC292 (Terry et al., 2005) were digested with BamHI-HF and HindIII-HF (New England BioLabs, Ipswich, MA) at 37°C for 1 hour and cleaned up with the QIAquick PCR Purification Kit (Qiagen, Valencia, CA) according to manufacturer instructions. Insert and vector were then ligated with T4 ligase (New England BioLabs) for 10 minutes at room temperature, inactivated at 65°C for 20 minutes, and stored at -20°C. 1 µl of the ligation mixture was transformed into OneShot TOP10

competent cells (Invitrogen, Carlsbad, CA) according to manufacturer instructions. Cells were plated on LB-ampicillin plates and incubated overnight at 37°C. Colonies were screened by colony PCR using primers AmgK_BamHI_F and MurU_HindIII_R. Plasmid pLC292-KU was purified from the resulting clone, HMJ_Ec_pLC292-KU, using the QIAprep Spin Miniprep Kit (Qiagen) according to manufacturer instructions. Recipient *H. pylori* containing a *aphA3sacB* cassette at the *rdxA* locus(LSH108 (Sycuro et al., 2010)) were transformed with the purified plasmid. Transformants were selected on sucrose plates and kanamycin sensitivity was verified. Genomic DNA was purified using the Wizard Genomic DNA Purification Kit (Promega, Fitchburg, WI) and insertion of AmgK MurU at *rdxA* was verified by PCR amplifying sequencing the locus using primers RdxA_F1P1 and RdxA_dnstm_RP2. The resulting confirmed strain was named HJH1.

Table 3. Primers used in this study

Primer name	**Sequence (5' to 3')**
AmgK_BamHI_F	GATAGGATCCTGACCCGCTTGACGGCTA
MurU_HindIII_R	GTATAAGCTTTCAGGCGCGCTCGC
RdxA_F1P1	CAATTGCGTTATCCCAGC
RdxA_dnstm_RP2	AAGGTCGCTTGCTCAATC
CcmA SDM mi R	AGACTAGATTGGATCATTCCCTATTTATTTTCAATTTTCT
CcmA SDM mi F	ATAAAGAAAGGAGCATCAGATGGCAATCTTTGATAACAAT
CcmA SDM up R	ATTGTTATCAAAGATTGCCATCTGATGCTCCTTTCTTTAT
CcmA SDM dn F	AGAAAATTGAAAATAAATAGGGAATGATCCAATCTAGTCT
CcmA SDM dn R	GCTCATTTGAGTGGTGGGAT
Csd1 F	GAGTCGTTACATTAATGTGCATATCT
SDM 155A F	ATTCTAAAAGCACGGTGGTGgcCGGACAAACCGGCTCGGTAG
SDM 155A R	CTACCGAGCCGGTTTGTCCGgcCACCACCGTGCTTTTAGAAT
SDM L110S F	TGGTGGAAAGGAAGGGGATTtcGATTGGGGAAACTCGCCCTA
SDM L110S R	TAGGGCGAGTTTCCCCAATCgaAATCCCCTTCCTTTCCACCA

Fosfomycin rescue with MurNAc

Overnight liquid cultures of HJH1 and parent strain LSH108 grown to 0.3-0.5 OD_{600}/ml were diluted in BB10, BB10 containing fosfomycin, or BB10 containing fosfomycin and MurNAc to yield cultures at 0.002

714 OD_{600}/ml, with 50 µg/ml fosfomycin, or 50 µg/ml fosfomycin and 4 mg/ml MurNAc, as appropriate.
715 Cultures were grown shaking in 5 ml polystyrene tubes. Samples were taken initially and after 12 hours
716 10 µl of culture was diluted into 30 µl of BB10 and a 10-fold dilution series was performed from this
717 initial dilution. 4 µl of each dilution for each experimental condition was spotted on plates and plates
718 were incubated 5-6 days.

719 **PG preps and analysis for D-Ala-alk and MurNAc-alk**

720 330 ml of liquid cultures were grown for six doublings to an optical density at 600 nm (OD_{600}) reading of
721 1 with 100 µg/ml D-alanine-alk ((R)-2-Amino-4-pentynoic acid, Boaopharma, Woburn, MA), 62.5 µg/ml
722 MurNAc-alk (synthesized and characterized as previously described (Liang et al., 2017), or no additions.
723 Cells were harvested and sacculi were purified as previously described (Blair et al., 2018). Briefly, cells
724 were harvested by centrifugation at 4°C, resuspended in PBS, and added dropwise to boiling 8% SDS.
725 SDS was then removed by ultracentrifugation and washing. Then sacculi were resuspended in 900 µl of
726 10 mM Tris HCl with 10 mM NaCl pH 7.0 and 100 µl of 3.2M imidazole pH 7.0 and incubated with 15 µl
727 α-amylase (10 mg/ml) (Sigma, St. Louis, MA) for 2 hours at 37°C and 20 µl Pronase E (10 mg/ml) (Fisher
728 Scientific, Pittsburgh, PA) for 1 hour at 60°C. 500 µl of 8% SDS was added and samples were boiled for 15
729 minutes. SDS was again removed by ultracentrifugation and washes with water. The purified PG was
730 suspended in 20 mM sodium phosphate pH 4.8 (D-Ala-alk samples) or 20 mM ammonium formate pH
731 4.8 (MurNAc-alk samples) and incubated overnight with 10 µg of cellosyl (kind gift from Hoechst,
732 Frankfurt am Main, Germany) at 37°C on a Thermomixer at 900 rpm. Following this incubation, the
733 samples were placed in a dry heat block at 100°C for 10 min and centrifuged at room temperature for 15
734 min at 16,000×g. The supernatant was retrieved. D-Ala-alk labeled digests were reduced with sodium
735 borohydride (Merck KGaA, Darmstadt, Germany) and separated by RP-HPLC, peaks collected and
736 analyzed using offline electrospray mass spectrometry as previously described (Bui et al., 2009).
737 MurNAc-alk labeled digests (non-reduced) were analyzed via injection onto a capillary (0.5 X 150 mm)
738 ACE Ultracore 2.5 super C18 column (Hichrom, Lutterworth, UK). The LC-MS instrument configuration
739 comprised a NanoAcquity HPLC system (Waters, Milford, MA) and QTOF mass spectrometer (Impact II,
740 Bruker, Billerica, MA). Buffer A was 0.1% formic acid (VWR, Lutterworth, UK) in water (VWR). Buffer B
741 was 0.1% formic acid in acetonitrile (VWR). RP-HPLC conditions were as follows: 0 % buffer B for 3 min,
742 1.5 % B at 20 min, 3.0 % B at 35 min, 15 %B at 45 min, 45% B at 50 min, followed by 2 min at 85% B and
743 finally 15 min re-equilibration at 0 %B. The flow rate was 0.02 ml/min and the capillary column
744 temperature was set at 35°C.
745 MS data was collected in positive ion mode, 50 – 2000 m/z, with capillary voltage and temperature

settings of 3200 V and 150°C respectively, together with a drying gas flow of 5 L/min and nebulizer pressure of 0.6 Bar. The resulting MS spectral data was analyzed using Compass DataAnalysis™ software (Bruker).

18-minute pulses with D-Ala-alk and MurNAc-alk

400 µl of HJH1 overnight liquid cultures in BB10 grown to 0.3-0.5 OD_{600}/ml was added to a 5 ml polystyrene round bottom tube and equilibrated in the 37°C Trigas incubator for 15 minutes before addition of the metabolic probe. 8 µl of a 200 mg/ml MurNAc-alk (synthesized and characterized as previously described (Liang et al., 2017)) stock in DMSO (final concentration = 4mg/ml) or 4 µl of a 100 mM stock of D-Ala-alk ((R)-2-Amino-4-pentynoic acid, Boaopharma) in DMSO was added to the culture. The culture was incubated for 18 minutes and growth was arrested by adding 4 µl of 10% sodium azide and placing cultures on ice for 5 minutes. Cells were transferred to a 1.5 ml microcentrifuge tube, pelleted in a microcentrifuge for 5 minutes at 5000 rpm, and resuspended in 1 ml Brucella broth. Paraformaldehyde was added to a final concentration of 4%. Cells were fixed at room temperature for 45 minutes, pelleted, and resuspended in 70% ethanol. Cells were permeabilized on ice for 30 minutes, pelleted, and resuspended in PBS. Cell suspensions density was normalized between samples using a hemocytometer and cells were spun onto clean glass coverslips at 500 rcf for 5 minutes in a Hettich Rotana 460R swinging bucket centrifuge. Click chemistry was performed on coverslips using the Click-iT Cell Reaction Buffer Kit (Invitrogen) according to manufacturer instructions (without BSA washes) with 8 µg/ml Alexa Fluor 555 Azide (Invitrogen). Coverslips were washed two times with 0.05% Tween-20 in PBS (PBST) for 10 minutes each and were then stained with 30 µg/ml WGA-Alexa Fluor 488 (Invitrogen) in PBS for 30 minutes at room temperature. Coverslips were washed an additional four times in PBST and mounted on slides with Prolong Diamond antifade (Invitrogen). Slides were cured for a week before imaging.

Immunofluorescence (CcmA-FLAG, CcmA, MreB)

Overnight liquid cultures in BB10 grown to 0.3-0.5 OD_{600}/ml were fixed at room temperature for 45 minutes with 4% paraformaldehyde. Cells were pelleted in a TOMY TX-160 micro centrifuge for 5 minutes at 5000 rpm and resuspended in 0.1% Triton X-100 in PBS for one hour at room temperature to permeabilize the cells. Cells were then pelleted in an Eppendorf microfuge at 2400 rpm for 10 minutes and resuspended in PBS. Cell suspensions density was normalized using a hemocytometer and cells were spun onto clean glass coverslips at 500 rcf for 5 minutes in a Hettich Rotana 460R swinging bucket centrifuge. Coverslips were stained with 30 µg/ml WGA-Alexa Fluor 555 (Invitrogen) in PBS for 30

minutes at room temperature, washed four times with 0.05% Tween-20 in PBS (PBST) for 10 minutes each, blocked for two hours with 5% goat serum (Sigma) in PBST at room temperature, and then incubated overnight at 4°C in primary antibody in 5% goat serum PBST. Mouse anti-FLAG M2 (Sigma), rabbit anti-CcmA (Blair et al., 2018), and CcmA preimmune serum were used at a 1:200 dilution. Rabbit anti-MreB and MreB preimmune serum (a gift from Dr. Hong Wu and Dr. Kouichi Sano (Nakano et al., 2012)) were used at a 1:500 dilution. After primary antibody incubation, coverslips were washed four times in PBST and incubated with 1:200 Alexa Fluor 488 anti-mouse (A-11029, Invitrogen) or 1:200 Alexa Fluor 488 anti-rabbit (A-11008, Invitrogen) in PBST for 45 minutes at room temperature. After secondary antibody incubation, coverslips were washed four times in PBST and mounted on slides with Prolong Diamond antifade (Invitrogen). Slides were cured for a week before imaging. For CcmA-FLAG immunofluorescence, strain JTH5 was used. JTH5 was generated by natural transformation HJH1 with genomic DNA from JTH3 (Blair et al., 2018) and selection on kanamycin blood plates. HJH1 was used as the corresponding no-FLAG control, as well as for the anti-MreB and MreB preimmune immunofluorescence. Wild-type LSH100 (Lowenthal et al., 2009) was used for anti-CcmA and CcmA preimmune immunofluorescence.

3D structured illumination imaging

Slides for cell surface curvature enrichment analysis were imaged on a DeltaVision OMX V4 BLAZE 3D microscope (GE Healthcare Life Sciences, Chicago, IL) equipped with Photometrics Evolve 512 emCCD cameras and a UPlanApo 100x/1.42 oil objective with oil matched for the sample refractive index. 512 x 512 pixel images were collected with 3 msec exposure and 170 EMCCD gain using a 100 mW 488 nm laser with 10% transmission. Z-plane images were acquired with 125 nm spacing. The remaining SIM microscopy was performed on a DeltaVision OMX-SR equipped with PCO scientific CMOS cameras, 488 nm and 568 nm lasers, and an Olympus 60x/1.42 U PLAN APO oil objective with oil matched for the sample refractive index. 512 x 512 pixel Z-plane images with 125 nm spacing and 3 µm thickness were collected. For D-Ala-alk and MurNAc-alk samples, images were collected with 5% 488 and 15% 568 laser power for 20 msec and 100 msec exposures, respectively. For MurNAc-alk samples, images were collected with 10% 488 and 15% 568 laser power for 2 msec and 80 msec exposures, respectively. For α-FLAG immunostained samples, images were collected with 10% 488 and 10% 568 laser power and 40 msec and 25 msec exposure, respectively. For α-MreB immunostained samples, images were collected with 10% 488 and 10% 568 laser power and 70 msec and 25 msec exposure, respectively. For α-CcmA immunostained samples, images were collected with 15% 488 and 15% 568 laser power and 30 msec and 40 msec exposure, respectively. Images were processed using included Softworx software. Figures

were generated by opening files in Fiji (Schindelin et al., 2012), adjusting brightness and contrast, and assembling in Adobe Photoshop. Scaling of maximum projection and Z-slice images are equal for all samples within a set (D-Ala-alk and mock; MurNAc-alk and mock; α-FLAG M2; α-MreB and preimmune serum; and α-CcmA and preimmune serum), with the exception of the I55A CcmA anti-CcmA and preimmune images, which were brightened in comparison to other anti-CcmA and preimmune images to compensate for the reduced expression of I55A CcmA. Scaling is equal for I55A CcmA anti-CcmA and preimmune images.

3D reconstructions and curvature enrichment

3D cell surfaces were generated from the 3D-SIM OMX software reconstructions using existing software [Morgenstein 2015, Bratton 2018, Bartlett 2017] with parameters optimized for the difference in imaging modality and file formats. This method minimizes the difference between the observed image and a forward convolution model of the true intensity distribution and the microscope's transfer function. While the images generated by 3D-SIM are not precisely equal to the convolution of the true intensity distribution, we consider the observed images as if they had been generated with an effective blurring function that we parameterize as a 3D Gaussian blur. For each individual cell, the reconstruction algorithm returns the 3D shape of the cell as a collection of vertex positions $\{V_i\}$ and a collection of faces defining which vertices are connected to each other. These faces and positions allow us to calculate geometric properties including the volume, surface area, local principle curvatures, etc. (Bratton et al., 2018; Rusinkiewicz, 2004). The Gaussian curvature at any point on the surface is the product of the principle curvatures and is therefore independent of the sign convention chosen for the principle curvatures. Following reconstruction, each cell surface undergoes a visual inspection quality control step. To estimate the diameter of each cell, we use the distance from each surface point to its nearest centerline point as a proxy for the local radius. The cell diameter is then the weighted average of twice the local radius, weighted by the surface area represented by each vertex.

In addition to the geometric properties of the surface, we calculate the intensity of a secondary fluorophore at the coordinates of the surface, for example D-Ala-alk, MurNAc-alk, or immunofluorescence. For each individual cell, the average surface concentration was calculated as the surface area weighted sum of the fluorescence at the surface divided by the total surface area of that cell. This normalization sets the concentration scale for the enrichment analysis; a value of one is the same concentration as if all the intensity was uniformly spread on the surface, concentrations greater than one are enriched and concentrations less than one are depleted. When considering the entire cell

surface, the normalization included all surface vertices. When only considering the sidewalls of the cell, we first removed all the vertices in the polar regions. These regions were defined as all the points on the surface whose nearest centerline was closer to the pole than 0.75 of the cell diameter (Figure 1B). Following normalization, we calculated the geometric enrichment in each individual cells by averaging the concentration across all the vertices of a particular Gaussian curvature. This enrichment profile was then averaged across the entire population of cells. We truncate the analysis to Gaussian curvatures which have sufficient representation (>4e-4). For error estimation, we report 90% confidence intervals from bootstrap analysis across cells and plot this interval, along with the mean, using cubic smoothing splines (Figure 6, lines). Each sample is the composite dataset from three biological replicates.

Determining helical fits of 3D centerlines

To examine the helical parameters of the cell centerlines, we adapted the helical fitting algorithm from Nievergelt (Nievergelt, 1997). The first step in the routine is to estimate a right-cylindrical surface on which all the data lie. This is defined by four parameters, three which define a vector parallel to the helical axis (X_a, Y_a, Z_a) and the cylinder diameter (D). The remaining four parameters are determined in a subsequent step. These define a point on the helix (X_o, Y_o, Z_o) and the helical pitch (P). The algorithm takes advantage of the speed of singular value decomposition (SVD) by framing the best fit as a linear algebra problem. The modifications that we made to the algorithm were in a preconditioning step as well as steps 2 and 3. The center of mass of the data was subtracted off from all the observations and then added back into X_0, Y_0, and Z_{0v}. For our real cells the two smallest singular values in step 2.3 are sometimes of similar magnitude and are both checked to see which right-singular vector is more consistent with a cylinder. The use of SVD instead of eigenvalue decomposition does not retain the right-handed convention of space forcing us to switch step 2.4 to an eigenvalue decomposition. In estimating the pitch of the helix in step 3.2, the algorithm by Nievergelt did not support helical data that covered more than one helical turn. This type of data presents a phase wrapping issue. To solve this issue, we first sorted the data by its projected position along the helical axis. We assumed that the relative phase difference between any two subsequent points was close to zero and calculated an absolute phase at each point by summing the relative phase differences along the whole curve. This then allowed us to calculate the relative slope of the helical phase. Here we again had to break from Nievergelt's SVD approach and used simple linear regression to retain the right-handed convention of space.

For each cell that was independently reconstructed, we estimate the best fit helical parameters for the centerline. Because we do not consider the orientation and offset of the helix to be shape parameters, we do not present any statistics on them. To estimate if the best fit helix was consistent with the centerline, we calculated the root mean squared deviation (RMSD) between the observed centerline coordinates and the best fit helix. One third (402/1137) of the cells had centerlines consistent with single helix. From the one third of the population that matched a single helix, we generated synthetic helical rods with the same helial parameters as each individual cell. From these, we compared the simulated and reconstructed cells in terms of their surface area, volume, volume of the convex hull, and Euclidean distance from pole to pole. If any of the parameters from the simulated cell deviated from the measured value by more than 10%, we excluded that cell from the analysis. In the end, we were left with almost 20% (231/1137) of the wild-type cells that were consistent with our model that cell shape is close to spherocylinder wrapped around a helical centerline.

Synthetic cells were generated using two major components, a helical centerline and a cylindrical coordinate system about that centerline. In cylindrical coordinates (R, θ, L), a cylinder with hemispherical endcaps has a simple form of a constant radius in the cylinder region and parabolic dependence in the endcaps. We then wrap the coordinate system around a helical axis by calculating the Frenet-Serret frame at each point of the helical centerline from the local tangent, normal, and their cross-product, the binormal. This wraps a fixed angular coordinate θ around the centerline, generating the helical rod surface of interest. However, these surfaces are still in a rectangular format, meaning that they are stored as three matrices {x,y,z} as a function of the (θ, L). This surface is resampled into a triangular approximation of the surface with approximately equilateral triangles using the surface reconstruction tools that we have previously developed (Bartlett et al., 2017; Bratton et al., 2018). Some geometric parameters, including the Gaussian curvature at each point on the surface and the surface area and the volume of the cells, can be calculated for both real cell reconstructions and the synthetic cells (Figure 3C-F, supplement 1C-E, and supplement 4, left column). For these, we defined the pole surface area as the surface within 0.75 cell diameters of the end). Because of their intrinsic unwrap coordinate system, synthetic cells have defined surface helical axes, which allows us to compute the length of the major and minor axes as well as the Gaussian curvature at these axes. Since the decrease in local diameter near the pole changes both the curvature and the length of the helical axis, we calculate the major and minor axis lengths and Gaussian curvatures from the central 50% of the cell, where the measurements are not influenced by the poles (Figure 3G-H and supplement 4, middle and right columns). Since decreasing the total length of the cell proportionally decreases the both sidewall

902 portion of the cell (including surface curvature properties) and the length of the major and minor axes
903 and since we present the axis length measurements as the ratio of the two axis lengths, we can justify
904 this approach. As shown in Figure 3 - supplement 4A (center and right columns), the length of the cell
905 has negligible influence on the distribution of surface curvatures and the ratio of major to minor axis
906 length, further validating our aggressive threshold for removing the ends of the cells for these
907 measurements.

908 **Purification of recombinant 6His-CcmA and variants**

909 Plasmids containing N-terminal 6-histadine fusions to WT CcmA (pKB62) and CcmA containing point
910 mutations were generated using site directed mutagenesis primers (Table 3) to generate CcmA I55A
911 (pKB69H; primers SDM 155A F and SDM I55A R) and CcmA L110S (pKB72D; primers SDM L110S F and
912 SDM L110S R). Plasmids were transformed into *E. coli* protein production host BL21. Strains were grown
913 overnight at 37°C in LB with 0.2% glucose and 100 µg/ml ampicillin. The next day, cells were diluted
914 1/1000 into fresh media without glucose, grown to mid-log (0.5-0.75), chilled on ice for 15 minutes, then
915 induced for protein expression by adding 1.0 mM IPTG, flasks were transferred to room temperature
916 and incubated with shaking for 3.5-4 hours. Cells were harvested by centrifugation and either used
917 immediately for protein purification or frozen at -80°C. For purification, cells were re-suspended in 2/5
918 culture volume of lysis buffer (25 mM Tris pH8.0, 2 M urea, 500 mM NaCl, 2% glycerol, 0.5 mg/mL
919 lysozyme) supplemented with ¼ EDTA-free protease inhibitor tablet (Pierce, Waltham, MA) and 2 U
920 Benzonase nuclease (EMD Millipore, Burlington, MA) and incubated at room temperature with gentle
921 rolling for 1 hour. After lysing, cells were sonicated at 20% power with 15 second pulses until all cells
922 were lysed. Lysates were cleared at 5000 x g at 4°C, then applied to equilibrated TALON metal affinity
923 resin (TaKaRa, Shiga, Japan) and incubated for 2 hours at room temperature with gentle rolling. The
924 protein bound to resin was washed twice with wash buffer (25 mM Tris pH8.0, 2 M urea, 500 mM NaCl,
925 2% glycerol, 7.5 mM imidazole), and proteins eluted from the resin using 25 mM Tris pH8.0, 2 M urea,
926 500 mM NaCl, 2% glycerol, 250 mM imidazole). Fractions were analyzed by SDS-PAGE for purity and
927 yield. Protein concentration was determined using a Nanodrop 1000 (Thermo Fisher Scientific, Waltham,
928 MA) using the Protein A280 program.

929 **CcmA point mutation strain construction in *H. pylori***

930 Strains containing CcmA point mutants were created based on previously published methods (Sycuro et
931 al., 2010). Briefly, PCR products were amplified from pKB69H (I55A) or pKB72D (L110S) using primers
932 CcmA SDM mi F and CcmA SDM mi R (Table 3). Those products were annealed using PCR SOEing

(Horton, 1995) to fragments amplified from WT *H. pylori* flanking the CcmA locus using primers Csd1F and CcmA SDM up R (upstream fragment, 810 bp flanking) and CcmA SDM dn F and CcmA SDM dn R (downstream fragment, 540 bp flanking). PCR product was transformed into a *catsacB ccmA* knockout strain LSH117 (LSH100 naturally transformed with KGH10 (Sycuro et al., 2010) genomic DNA) and colonies resistant to sucrose and susceptible to chloramphenicol were validated using PCR and Sanger. Single clones of colonies containing correct mutations were used for all experiments.

Immunoblotting *H. pylori* extracts

Whole cell extracts were prepared by harvesting 1.0 OD_{600} of log phase (0.3-0.7 OD_{600}) *H. pylori* by centrifugation for 2 minutes at max speed in a microcentrifuge and resuspending in 2x protein sample buffer (62.5 mM Tris pH 8, 2% SDS, .02% bromophenol blue, 20% glycerol) at 10.0 OD_{600} per ml and boiled for 10 minutes. Whole cell extracts were separated on 4-15% gradient BioRad TGX gels by SDS-PAGE and transferred onto PVDF membranes using the BioRad Turbo-transfer system according to the manufacturer's instructions (BioRad, Hercules, CA). Membranes were blocked for 2 hours at room temperature with 5% non- fat milk in TBST (0.5 M Tris,1.5 M NaCl, pH 7.6, plus 0.05% Tween 20). Membranes were incubated with primary antibody for 2 hours at room temperature with 1:10,000 α-CcmA primary antibody or 1:20,000 dilution for α-Cag3 (Pinto-Santini and Salama, 2009), in TBST. Six washes with TBST over a 30 minute period were followed by a 1 hour incubation at room temperature with horseradish peroxidase- conjugated anti-rabbit immunoglobulin G (Santa Cruz Biotechnology, Dallas, TX) antibody at 1:20,000 dilution in TBST. After six washes with TBST washes over a 30 minute period, antibody detection was performed with ECL Plus (Pierce) detection kit, following the manufacturer's protocol and imaged with the BioRad Gel Documentation System.

2D *H. pylori* quantitative cell shape analysis

Phase-contrast microscopy was performed on cells grown in shaken liquid culture until mid-log phase (OD_{600} 0.3.-0.6), fixed in a 4% PFA/PBS + 10% glycerol solution and mounted on glass slides. Resulting images were acquired using a Nikon TE 200 microscope with at 100X oil-immersion objective and Nikon CoolSNAP HQ CCD camera controlled by MetaMorph software (MDS Analytical Technologies, Sunnyvale, CA). Images were thresholded using the ImageJ software package. Quantitative analysis of thresholded images were used to measure both side curvature and central axis length with the CellTool software package as described previously (Sycuro et al., 2010).

962 **Transmission electron microscopy**

963 For TEM 10 µM WT, I55A, or L110S CcmA was dialyzed overnight at 4°C against 25 mM Tris pH 8. The
964 proteins were applied to glow-discharged carbon-coated grids and negatively stained with 0.75% uranyl
965 acetate. Images were acquired with JEOL 1400 transmission electron microscope using a Gatan
966 UltraScan 1000xp camera with 2K x 2K resolution.

967 **Acknowledgements**

968 This research was supported in part by US National Institutes of Health R01 AI136946 (NRS), U01
969 CA221230 (CLG and NRS), T32 CA009657 (KMB), T32 GM95421 (SRS), T32 GM008550 (KED), the FHCRC
970 Cellular Imaging and Genomics and Bioinformatics Shared Resources of the NCI Center Support Grant
971 P30 CA015704, the Stanford Imaging Award Number 1S10OD01227601 from the National Center for
972 Research Resources (NCRR), the Life Sciences Research Foundation (EK), and the Wellcome Trust grant
973 101824/Z/13/Z (WV).This work was supported by the National Science Foundation Graduate Research
974 Fellowship Program under Grant No. DGE-0718124 (JAT) and DGE-1256082 (JAT and KMB), the
975 Department of Defense (DoD) through the National Defense Science & Engineering Graduate Fellowship
976 (NDSEG) Program (JAT), and the GO-MAP Graduate Opportunity Program Research Assistantship Award
977 (GOP Award) (SRS). This work was supported by National Science Foundation PHY-1734030 (BPB and
978 JWS), the Glenn Centers for Aging Research (BPB) and National Institutes of Health NIH R21 AI121828
979 (BPB and JWS).

980 The opinions, findings, and conclusions or recommendations expressed in this material contents are
981 solely the responsibility of the authors and do not necessarily represent the official views of the NCRR,
982 the National Institutes of Health, the Department of Defense, or the National Science Foundation. The
983 authors have no conflicts of interest to report.

984 We would like to thank Laura Sycuro for strain construction; Desirée Yang for MreB knockout attempts;
985 Patrina Pellett (GE Healthcare) for assistance with OMX imaging; and Sloan Siegrist (University of
986 Massachusetts Amhurst) for the D-alanine-D-alanine-alkyne and D-alanine-alkyne-D-alanine reagents.
987 We kindly thank Dr. Hong Wu and Dr. Kouichi Sano (Osaka Medical College) for the anti-MreB and
988 corresponding preimmune sera used in this study; Anson Chan (University of British Columbia) for
989 consultation on CcmA point mutants; and Zachary Jones for assistance in synthesizing the MurNAc
990 sugars.

991

992 **References**

993 Bartlett TM, Bratton BP, Duvshani A, Miguel A, Sheng Y, Martin NR, Nguyen JP, Persat A, Desmarais SM,
994 VanNieuwenhze MS, Huang KC, Zhu J, Shaevitz JW, Gitai Z. 2017. A Periplasmic Polymer Curves
995 *Vibrio cholerae* and Promotes Pathogenesis. *Cell* **168**:172–185.e15. doi:10.1016/j.cell.2016.12.019

996 Blair KM, Mears KS, Taylor JA, Fero J, Jones LA, Gafken PR, Whitney JC, Salama NR. 2018. The
997 *Helicobacter pylori* cell shape promoting protein Csd5 interacts with the cell wall, MurF, and the
998 bacterial cytoskeleton. *Mol Microbiol* **110**:114–127. doi:10.1111/mmi.14087

999 Bonis M, Ecobichon C, Guadagnini S, Prévost MC, Boneca IG. 2010. A M23B family metallopeptidase of
1000 *Helicobacter pylori* required for cell shape, pole formation and virulence. *Mol Microbiol* **78**:809–
1001 819. doi:10.1111/j.1365-2958.2010.07383.x

1002 Bratton BP, Shaevitz JW, Gitai Z, Morgenstein RM. 2018. MreB polymers and curvature localization are
1003 enhanced by RodZ and predict *E. coli*'s cylindrical uniformity. *Nat Commun* **9**. doi:10.1038/s41467-
1004 018-05186-5

1005 Bui NK, Gray J, Schwarz H, Schumann P, Blanot D, Vollmer W. 2009. The peptidoglycan sacculus of
1006 *Myxococcus xanthus* has unusual structural features and is degraded during glycerol-induced
1007 myxospore development. *J Bacteriol* **191**:494–505. doi:10.1128/JB.00608-08

1008 Cabeen MT, Charbon G, Vollmer W, Born P, Ausmees N, Weibel DB, Jacobs-Wagner C. 2009. Bacterial
1009 cell curvature through mechanical control of cell growth. *EMBO J* **28**:1208–1219.
1010 doi:10.1038/emboj.2009.61

1011 Correa P. 1988. Perspectives in Cancer Research A Human Model of Gastric Carcinogenesis. *Nutrition*
1012 3554–3560.

1013 Costa K, Bacher G, Allmaier G, Dominguez-Bello MG, Engstrand L, Falk P, De Pedro MA, García-del
1014 Portillo F. 1999. The morphological transition of *Helicobacter pylori* cells from spiral to coccoid is
1015 preceded by a substantial modification of the cell wall. *J Bacteriol* **181**:3710–3715.

1016 Ghuysen JM. 1991. Serine beta-lactamases and penicillin-binding proteins. *Annu Rev Microbiol* **45**:37–
1017 67. doi:10.1146/annurev.mi.45.100191.000345

1018 Gisin J, Schneider A, Nägele B, Borisova M, Mayer C. 2013. A cell wall recycling shortcut that bypasses

peptidoglycan *de novo* biosynthesis. *Nat Chem Biol* **9**:491–493. doi:10.1038/nchembio.1289

Goodwin A, Kersulyte D, Sisson G, Veldhuyzen Van Zanten SJO, Berg DE, Hoffman PS. 1998. Metronidazole resistance in *Helicobacter pylori* is due to null mutations in a gene (*rdxA*) that encodes an oxygen-insensitive NADPH nitroreductase. *Mol Microbiol* **28**:383–393. doi:10.1046/j.1365-2958.1998.00806.x

Höltje J V. 1998. Growth of the stress-bearing and shape-maintaining murein sacculus of *Escherichia coli*. *Microbiol Mol Biol Rev* **62**:181–203.

Horton RM. 1995. PCR-mediated recombination and mutagenesis - SOEing together tailor-made genes. *Mol Biotechnol* **3**:93–99. doi:10.1007/BF02789105

Humbert O, Salama NR. 2008. The *Helicobacter pylori* HpyAXII restriction-modification system limits exogenous DNA uptake by targeting GTAC sites but shows asymmetric conservation of the DNA methyltransferase and restriction endonuclease components. *Nucleic Acids Res* **36**:6893–6906. doi:10.1093/nar/gkn718

Hussain S, Wivagg CN, Szwedziak P, Wong F, Schaefer K, Izoré T, Renner LD, Holmes MJ, Sun Y, Bisson-Filho AW, Walker S, Amir A, Löwe J, Garner EC. 2018. MreB filaments align along greatest principal membrane curvature to orient cell wall synthesis. *Elife* **7**:e32471. doi:10.7554/eLife.32471

Jackson KM, Schwartz C, Wachter J, Rosa PA, Stewart PE. 2018. A widely conserved bacterial cytoskeletal component influences unique helical shape and motility of the spirochete *Leptospira biflexa*. *Mol Microbiol* **108**:77–89. doi:10.1111/mmi.13917

Kühn J, Briegel A, Mörschel E, Kahnt J, Leser K, Wick S, Jensen GJ, Thanbichler M. 2010. Bactofilins, a ubiquitous class of cytoskeletal proteins mediating polar localization of a cell wall synthase in *Caulobacter crescentus*. *EMBO J* **29**:327–339. doi:10.1038/emboj.2009.358

Kuru E, Hughes HV, Brown PJ, Hall E, Tekkam S, Cava F, De Pedro MA, Brun Y V., Vannieuwenhze MS. 2012. In situ probing of newly synthesized peptidoglycan in live bacteria with fluorescent D-amino acids. *Angew Chemie - Int Ed* **51**:12519–12523. doi:10.1002/anie.201206749

Liang H, DeMeester KE, Hou CW, Parent MA, Caplan JL, Grimes CL. 2017. Metabolic labelling of the carbohydrate core in bacterial peptidoglycan and its applications. *Nat Commun* **8**:1–11. doi:10.1038/ncomms15015

1047 Liechti GW, Kuru E, Hall E, Kalinda A, Brun Y V., Vannieuwenhze M, Maurelli AT. 2014. A new metabolic
1048 cell-wall labelling method reveals peptidoglycan in *Chlamydia trachomatis*. *Nature* **506**:507–510.
1049 doi:10.1038/nature12892

1050 Lowenthal AC, Hill M, Sycuro LK, Mehmood K, Salama NR, Ottemann KM. 2009. Functional analysis of
1051 the *Helicobacter pylori* flagellar switch proteins. *J Bacteriol* **191**:7147–7156. doi:10.1128/JB.00749-
1052 09

1053 Meeske AJ, Riley EP, Robins WP, Uehara T, Mekalanos JJ, Kahne D, Walker S, Kruse AC, Bernhardt TG,
1054 Rudner DZ. 2016. SEDS proteins are a widespread family of bacterial cell wall polymerases. *Nature*
1055 **537**:634–638. doi:10.1038/nature19331

1056 Morgenstein RM, Bratton BP, Nguyen JP, Ouzounov N, Shaevitz JW, Gitai Z. 2015. RodZ links MreB to cell
1057 wall synthesis to mediate MreB rotation and robust morphogenesis. *Proc Natl Acad Sci* **112**:12510–
1058 12515. doi:10.1073/pnas.1509610112

1059 Nakano T, Aoki H, Wu H, Fujioka Y, Nakazawa E, Sano K. 2012. Fine visualization of filamentous
1060 structures in the bacterial cytoplasm. *J Microbiol Methods* **90**:60–64.
1061 doi:10.1016/j.mimet.2012.03.016

1062 Nievergelt Y. 1997. Fitting helices to data by total least squares. *Comput Aided Geom Des* **14**:707–718.
1063 doi:10.1016/S0167-8396(96)00058-1

1064 Pinto-Santini DM, Salama NR. 2009. Cag3 is a novel essential component of the *Helicobacter pylori* Cag
1065 Type IV secretion system outer membrane subcomplex. *J Bacteriol* **191**:7343–7352.
1066 doi:10.1128/JB.00946-09

1067 Rusinkiewicz S. 2004. Estimating curvatures and their derivatives on triangle meshes. *Proc - 2nd Int Symp*
1068 *3D Data Process Vis Transm 3DPVT 2004* 486–493. doi:10.1109/TDPVT.2004.1335277

1069 Sauvage E, Kerff F, Terrak M, Ayala JA, Charlier P. 2008. The penicillin-binding proteins: Structure and
1070 role in peptidoglycan biosynthesis. *FEMS Microbiol Rev* **32**:234–258. doi:10.1111/j.1574-
1071 6976.2008.00105.x

1072 Schindelin J, Arganda-Carreras I, Frise E, Kaynig V, Longair M, Pietzsch T, Preibisch S, Rueden C, Saalfeld
1073 S, Schmid B, Tinevez JY, White DJ, Hartenstein V, Eliceiri K, Tomancak P, Cardona A. 2012. Fiji: An
1074 open-source platform for biological-image analysis. *Nat Methods* **9**:676–682.

1075 doi:10.1038/nmeth.2019

1076 Shi C, Fricke P, Lin L, Chevelkov V, Wegstroth M, Giller K, Becker S, Thanbichler M, Lange A. 2015.
1077 Atomic-resolution structure of cytoskeletal bactofilin by solid-state NMR. *Sci Adv* **1**:1–6.
1078 doi:10.1126/sciadv.1501087

1079 Siegrist MS, Whiteside S, Jewett JC, Aditham A, Cava F, Bertozzi CR. 2013. D-amino acid chemical
1080 reporters reveal peptidoglycan dynamics of an intracellular pathogen. *ACS Chem Biol* **8**:500–505.
1081 doi:10.1021/cb3004995

1082 Smeets LC, Bijlsma JJE, Boomkens SY, Vandenbroucke-Grauls CMJE, Kusters JG. 2000. *comH*, a Novel
1083 Gene Essential for Natural Transformation of *Helicobacter pylori*. *J Bacteriol* **182**:3948–3954.
1084 doi:10.1128/jb.182.14.3948-3954.2000

1085 Specht M, Schätzle S, Graumann PL, Waidner B. 2011. *Helicobacter pylori* possesses four coiled-coil-rich
1086 proteins that form extended filamentous structures and control cell shape and motility. *J Bacteriol*
1087 **193**:4523–4530. doi:10.1128/JB.00231-11

1088 Sycuro LK, Pincus Z, Gutierrez KD, Biboy J, Stern CA, Vollmer W, Salama NR. 2010. Peptidoglycan
1089 crosslinking relaxation promotes *Helicobacter pylori*'s helical shape and stomach colonization. *Cell*
1090 **141**:822–833. doi:10.1016/j.cell.2010.03.046

1091 Sycuro LK, Rule CS, Petersen TW, Wyckoff TJ, Sessler T, Nagarkar DB, Khalid F, Pincus Z, Biboy J, Vollmer
1092 W, Salama NR. 2013. Flow cytometry-based enrichment for cell shape mutants identifies multiple
1093 genes that influence *Helicobacter pylori* morphology. *Mol Microbiol* **90**:869–883.
1094 doi:10.1111/mmi.12405

1095 Sycuro LK, Wyckoff TJ, Biboy J, Born P, Pincus Z, Vollmer W, Salama NR. 2012. Multiple peptidoglycan
1096 modification networks modulate *Helicobacter pylori*'s cell shape, motility, and colonization
1097 potential. *PLoS Pathog* **8**. doi:10.1371/journal.ppat.1002603

1098 Terry K, Williams SM, Connolly L, Ottemann KM. 2005. Chemotaxis plays multiple roles during
1099 *Helicobacter pylori* animal infection. *Infect Immun* **73**:803–811. doi:10.1128/IAI.73.2.803-811.2005

1100 Tomb JF, White O, Kerlavage AR, Clayton RA, Sutton GG, Fleischmann RD, Ketchum KA, Klenk HP, Gill S,
1101 Dougherty BA, Nelson K, Quackenbush J, Zhou L, Kirkness EF, Peterson S, Loftus B, Richardson D,
1102 Dodson R, Khalak HG, Glodek A, McKenney K, Fitzegerald LM, Lee N, Adams MD, Hickey EK, Berg

1103 DE, Gocayne JD, Utterback TR, Peterson JD, Kelley JM, Cotton MD, Weidman JM, Fujii C, Bowman
1104 C, Watthey L, Wallin E, Hayes WS, Borodovsky M, Karp PD, Smith HO, Fraser CM, Craig Venter J.
1105 1997. The complete genome sequence of the gastric pathogen *Helicobacter pylori*. *Nature*
1106 **388**:539–547. doi:10.1038/41483

1107 Typas A, Banzhaf M, Gross CA, Vollmer W. 2012. From the regulation of peptidoglycan synthesis to
1108 bacterial growth and morphology. *Nat Rev Microbiol* **10**:123–136. doi:10.1038/nrmicro2677

1109 Ursell TS, Nguyen J, Monds RD, Colavin A, Billings G, Ouzounov N, Gitai Z, Shaevitz JW, Huang KC. 2014.
1110 Rod-like bacterial shape is maintained by feedback between cell curvature and cytoskeletal
1111 localization. *Proc Natl Acad Sci* **111**:E1025–E1034. doi:10.1073/pnas.1317174111

1112 Vasa S, Lin L, Shi C, Habenstein B, Riedel D, Kühn J, Thanbichler M, Lange A. 2015. β-Helical architecture
1113 of cytoskeletal bactofilin filaments revealed by solid-state NMR. *Proc Natl Acad Sci* **112**:E127–E136.
1114 doi:10.1073/pnas.1418450112

1115 Waidner B, Specht M, Dempwolff F, Haeberer K, Schaetzle S, Speth V, Kist M, Graumann PL. 2009. A
1116 novel system of cytoskeletal elements in the human pathogen *Helicobacter pylori*. *PLoS Pathog* **5**.
1117 doi:10.1371/journal.ppat.1000669

1118 Yang DC, Blair KM, Taylor JA, Petersen TW, Sessler T, Tull CM, Leverich C, Collar AL, Wyckoff TJ, Biboy J,
1119 Vollmer W, Salama NR. 2019. A genome-wide *Helicobacter pylori* morphology screen uncovers a
1120 membrane spanning helical cell shape complex. *J Bacteriol* In revision

1121 Yoshiyama H, Nakazawa T. 2000. Unique mechanism of *Helicobacter pylori* for colonizing the gastric
1122 mucus. *Microbes Infect* **2**:55–60. doi:10.1016/S1286-4579(00)00285-9

1123 Zhao H, Patel V, Helmann JD, Dörr T. 2017. Don’t let sleeping dogmas lie: new views of peptidoglycan
1124 synthesis and its regulation. *Mol Microbiol* **106**:847–860. doi:10.1111/mmi.13853

1125

Appendix 1

Selecting a subset of wild-type cells whose geometry is consistent with the four parameter model of helical-rod shape. We generated a set of simulated helical cells based on the three-dimensional reconstructions of the wild-type population shown in Figure 2. Inputs to this simulation are the measured pole-pole cell lengths along the curved centerlines (Figure 3A and C, gray); the diameters of the cells (Figure 3A and C, purple); the helical pitches of the centerlines (Figure 3A and C, pink); and the helical diameters of the centerlines (Figure 3A and C, green). To determine the helical pitch and radius from each reconstructed cell, we borrowed heavily from previous algorithms designed to calculate the best fit helix to a set of observations (Nievergelt, 1997). We modified these algorithms to accommodate helices longer than one helical repeat and to allow the pitch to be a signed value, with positive pitches corresponding to right-handed helices and negative to left-handed ones. Not all centerlines fit well to a single helical fit as some centerlines have kinks or variable pitch along their long axis. We calculated the relative error of the helical fit as the root mean squared deviation (RMSD) of the error in the fit to the RMSD between two subsequent points along the centerline. This relative error is unitless; we set a threshold value of two for satisfactory fits (Figure 3 - supplement 1A and 2). About one quarter of the centerlines had a good fit to a single helix (402/1137). Wild type *H. pylori* cells have been shown to be right handed (Yoshiyama and Nakazawa, 2000). Our algorithm finds that 96% of the cells with satisfactory fits are right handed (387/402). Infrequently (15/402), the algorithm returned a left-handed helix as the best fit. Upon visual inspection, none of these centerlines were globally left-handed and were thus discarded.

From the four calculated 3D shape parameters, we generated synthetic cells to mimic the original wild-type population. Just as we ignored cells whose centerlines were not well fit by a single helix, we also removed cells whose simulated counterpart differed from the real cell reconstruction by more than 10% in surface area, volume, volume of the convex hull, or Euclidean distance from pole to pole. For roughly 20% of the total wild-type population (231/1137), the observed geometry of the cell was consistent with the simple four parameter model (see Methods and Figure 3 - supplement 1A and B). It is not reasonable to look at the distribution of helical parameters for centerlines that do not have satisfactory fits. The distribution of cell lengths, cell diameters, and surface curvatures for the entire population and the population subset are closely matched (Figure 3- supplement 1C-E), indicating that the subset adequately represents the population. Both wild-type and synthetic cells share a multimodal distribution of Gaussian curvatures with peaks around 5 μm^{-2} and between -5 and -10 μm^{-2}. However, there is a

notable difference in the widths and magnitudes of these peaks between the wild-type and corresponding synthetic cells, consistent with the fact that, unlike real cells, the synthetic cell surfaces are perfectly smooth.

Using this subset of simulated cells, we then proceeded to characterize the major and minor helical axes. Because we simulated these cells based on a model of a cylinder wrapped and twisted about a helical axis, they inherently have a natural unwrap helical coordinate system (Figure 3A and supplement 1A and 2). We chose to set the unwrap angle of the major helical axis to 0° and the minor helical axis to 180° allowing us to measure the relative length of the major to minor helical axes as well as measure the average Gaussian curvature along the helical axes. The average Gaussian curvature at the major axis is 5 ± 1 μm^{-2}, and the average Gaussian curvature at the minor axis is -11 ± 4 μm^{-2}. There was substantially more variation in the average curvature at the minor axis than at the major axis (Figure 3H).